# FLUIDIC DRIVEN DIGITAL CLAY

A Thesis
Presented to
The Academic Faculty

by

James Davis Garth

In Partial Fulfillment
of the Requirements for the Degree
Master of Science

George W. Woodruff School of Mechanical Engineering
Georgia Institute of Technology
December 2006

# FLUIDIC DRIVEN DIGITAL CLAY

Approved by:

Dr. Ari Glezer, Advisor
School of Mechanical Engineering
*Georgia Institute of Technology*

Dr. Wayne Book
School of Mechanical Engineering
*Georgia Institute of Technology*

Dr. David Rosen
School of Mechanical Engineering
*Georgia Institute of Technology*

Date Approved: 12/30/06

# ACKNOWLEDGEMENTS

This work would not have been possible without the direction and technical guidance of my advisor Dr. Ari Glezer. The support and instruction of Dr. Wayne Book and Dr. David Rosen as members of my thesis reading committee is also greatly appreciated. The help of JD Huggins was instrumental in the realization of the 5x5 array of actuators. The financial support of the National Science Foundation (grant number 0121663) and the George W. Woodruff School of Mechanical Engineering is also gratefully acknowledged. The support of my family has been a priceless constant not only in my time at Georgia Tech but throughout my life.

# TABLE OF CONTENTS

# LIST OF TABLES

# LIST OF FIGURES

# LIST OF SYMBOLS AND ABBREVIATIONS

| | |
|---|---|
| TB1 | Test bed number one |
| TB2 | Test bed number two |
| VCT | Variable Core Transformer |
| ODMS | Optical Displacement Measurement System |
| FA | Fluidic Actuator |
| V1 | Valve used for downward actuation |
| V2 | Valve used for upward actuation |
| T1 | Pressure transducer 1 |
| T2 | Pressure transducer 2 |
| T3 | Pressure transducer 3 |
| NO | Normally Open valve port |
| NC | Normally Closed valve port |
| SLA | Stereolithography |
| HP Res | High Pressure reservoir |
| LP Res | Low Pressure reservoir |
| PSD | Position Sensitive Device |
| FS | Full Scale |
| LVDT | Linear Variable Differential Transformer |
| $\Phi_B$ | Magnetic flux |
| $d\vec{A}$ | Differential area |
| $\vec{B}$ | Magnetic field |
| $e_B$ | Bias error |
| $P_T$ | Known position |
| $P_S$ | Measured position |
| $\theta$ | Angle between magnetic field and differential area |
| $\varepsilon$ | Electromotive force |
| N | Turns of a transformer |
| $n_2$ | Number of turns in secondary coil |
| $\mu_0$ | Permeability of free space |
| $\mu_r$ | Relative permeability of material |
| A | Cross sectional area of coil |
| $l$ | Length of coil |
| $V_1$ | Voltage in “upper” secondary coil |
| $V_2$ | Voltage in “lower” secondary coil |
| $V_{out}$ | Output voltage |
| D1 | Diode one |
| D2 | Diode two |
| AC | Alternating current |
| DC | Direct current |
| Vpp | Volts peak-to-peak |

| | |
|---|---|
| $S_x$ | Standard deviation |
| $e_{overall}$ | Overall error |
| PI | Proportional Integral |
| d(t) | Desired controller output |
| e(t) | System error |
| c(t) | Controller output |
| a(t) | System output |
| $K_P$ | Proportional gain |
| $K_I$ | Integral gain |
| TTL | Transistor-transistor logic |
| $f_{teflon}$ | Friction due to Teflon top seal |
| $f_{inertia}$ | Friction due to viscous losses |
| $f_{side}$ | Friction due to side loading on piston head |
| $(pA)_u$ | Force in upper cylinder cavity |
| $(pA)_l$ | Force in lower cylinder cavity |
| $a_{piston}$ | Acceleration of piston |

# SUMMARY

Digital Clay is a tactile array of linear fluidic actuators which provide distributed sensing and position control through the use of an embedded position sensor. The actuator implementation is achieved by two-way hydraulically-driven pistons which are integrated with computer controlled valves. Each actuator is connected to an underlying base plate which is in fluidic communication with high and low pressure reservoirs. The research focuses on the aspects of the fluidics necessary to operate the actuators and control actuation of Digital Clay. The main objectives of this work are the characterization of the fluid flow through the system and the design and implementation of an embedded inductance-based position sensor. Each actuator in Digital Clay is individually addressable and is controlled through the use of a closed-loop proportional integral controller with position feedback from the embedded inductance-based sensor. Also presented in this work is the characterization of an individual fluidic actuator and the realization of a 5x5 tactile array of actuators.

# CHAPTER 1

# INTRODUCTION

Human/computer interaction is largely limited to the senses of sight and hearing through the use of a keyboard and a mouse. However, adding the sense of touch can greatly increase the effectiveness of communication between a computer and its user, especially in cases where the user is visually impaired (Linvill 1966). The sense of touch is an efficient way to communicate information pertaining to the shape, rigidity, and surface characteristics of an object.

Digital Clay (Rossignac 2003) is a human computer interface that allows both physical and mathematical interaction between a computer and its user. The name "Digital Clay" is derived from the combination of the shape manipulation capabilities of a sculptor's clay with the representation capabilities of digital display. This fusion of capabilities provides a device which bridges the gap of human computer interaction by adding the sense of touch; allowing two-way haptic communication of an object's shape, surface characteristics, and other tactile qualities in real time.

Most people assert that visual feedback is more important than somesthetic feedback, however, the few documented cases where people have lost their sense of touch have shown drastic debilitating results (Robles-De-La-Torre 2006) which are not present in cases of visual impairment; indicating that the importance of a person's sense of touch is often underestimated. The sense of touch is extremely important in everyday life and its

addition to computer interfaces can greatly enhance the interactions that people have with computers.

The present work focuses on the aspects of the fluidics necessary to operate the actuators and control actuation of Digital Clay. The main objectives of this work are the characterization of the fluid flow through the system and the design and implementation of an embedded inductance-based position sensor. Section 1.1 outlines research in the area of haptic interfaces as they apply to Digital Clay. Section 1.2 provides a number of tactile arrays which have been developed in the past forty years. Presented in section 1.3 are various fluidic-based tactile arrays. Section 1.4 describes the two versions of Digital Clay developed at Georgia Tech and the specific differences which separate the design presented here with those presented in sections 1.1-1.3.

## 1.1 Haptic Interfaces

A haptic interface is an interface that refers to manual interactions with the environment (Srinivasan 1997), such as exploration for extraction of information about the environment or manipulation for modifying the environment. Significant prior work has been conducted in the area of haptic interfaces, the earliest of which was a haptic device known as a teleoperator machine, (Yong 1998) which extends a person's sensing and/or manipulation capabilities to a remote location. Teleoperator machines span a wide range of functionality ranging from a simple tong to a sophisticated nuclear waste handling device. Early teleoperator machines consisted of linkages which kinematially connected the user (master) to a remote location (slave) (Goertz 1952). Goertz's manipulators

consisted of a system of tubes, cables, and pulleys which allowed the slave side of the manipulator to track the master. Using a hand-held controller and a set of tongs displayed the same manipulation on the slave side. This system, developed in 1945, was used in the precise handling of radioactive materials at Argonne National Laboratory (Goertz 1952; Hull 1952; Goertz 1954). As reported by Hull, (1952) when the master and slave sides of Goertz's manipulator were geometrically connected, the user had adequate force feedback to perform needed tasks naturally (Hull 1952). However, the distance between the master and the slave is limited by the physical construction of the mechanical linkages.

The first servo-controlled teleoperator was developed in 1947 (Goertz 1954). This design featured a 6 degree of freedom wrist joint which was actuated by 6 individual on-off switches. A set of tongs on the slave side was operated by a hydraulic system which allowed the user to feel the gripping force through the fluidic connections. While this design proved the concept of servo-operated manipulators, it had several shortcomings. Because of its on-off nature this manipulator was awkward to control (Goertz 1952) and only employed haptic feedback on the tongs but not the position of the slave arm. This means that the operator did not have a feel for the inertia of the manipulated item because the operator only interacted with the item through a set of switches. Before the introduction of servomotors, users were physically connected to a remote location and could, therefore, feel the object that they were manipulating through the force feedback of mechanical linkages. While introduction of servomotors allowed teleoperation to be conducted across greater distances the users did not have physical force feedback from

the mechanical linkage and had to rely on sensors installed on the slave side of the teleoperator (Kumar 2001). Early teleoperators allowed people to manipulate objects in a remote location, but they did not provide adequate capabilities for sensing and altering the shape of curves and surfaces.

Telepresence is a state which is achieved when sufficient information about the teleoperator and the remote environment are effectively communicated to the operator in such a way that the operator feels physically present at a remote site (Stone 2001). One of the more compelling ways to create telepresence is to employ a virtual reality environment (Jaron Lanier 1994), which is a 3-D computer-generated world that can be entered with the aid of goggle-mounted monitors and data-sensing clothing (Perry 1994). However, more recent definitions do not require the use of goggles or special clothing and explicitly state the need for the user to be able to interact with the virtual reality environment in real time (Zhu 2005).

The idea of fusing virtual reality environments with haptic interfaces to achieve telepresence has led to numerous simulators for military, medical, and industrial applications. In 2005, Kron and Schmidt (Kron 2005) developed a haptic telepresent robot for safe land mine disposal. The operators of this system place their hands into a set of gloves which haptically control two arms on a remote robot. All of the 20 subjects that were used to evaluate the device were able to perform the required simulated mine disposal without complications. However, while the same task can be completed by hand in less than 60 seconds, the average time of completion of the subjects was approximately

800 seconds (Kikuuwe 2004). Due to the innovations and widespread acceptance of minimally invasive surgery, a growing number of surgeons are isolated from the operation site and are limited to visual feedback through cameras, while obtaining gross motion and force feedback through long instrument handles (Howe 1995). Amato discusses the use and potential implications of several different surgical simulators ranging from routine catheter injections to more complicated colonoscopy and lung biopsy simulators (Amato 2001) whereby haptic interfaces drastically increase the sense of reality during simulation. Project GROPE was developed for haptic interaction with protein molecules (Brooks 1990). GROPE uses a modified manipulator from Argonne National Laboratory and a sophisticated graphics display to allow users to interact with protein models and test different molecular docking configurations. Many tests were run with and without haptic feedback with a wide variety of test subjects. The subjects which conducted the tests with the aid of the haptic feedback from GROPE completed the assigned tasks 1.75-2.2 times faster (Brooks 1990) and with greater accuracy than those subjects which used the same manipulator without haptic feedback.

## 1.2 Tactile Arrays

A Tactile Array is a device which typically consists of a planar arrangement of linear actuators and/or sensors acting perpendicular to that plane (Zhu 2005). Many finger tip sized tactile arrays have been developed for purposes ranging from medical palpation to reading aids for the blind (Linvill 1966; Fearing 1997). Finger-tip sized tactile arrays can range in size from a 1 mm square composed of an 8 x 8 element array (Gray 1996) to a 25 mm diameter cylinder containing 3 x 16 elements (Fearing 1997). Other large scale

tactile arrays have been created for shape recognition and interaction (Iwata 2001; Zhu 2005).

A study conducted at an Association for Computing Machinery's Special Interest Group on Graphics and Interactive Techniques (ACM SIGGRAPH) conference (Iwata 2001) showed that 85% of the participants used multiple fingers or their palms to interact with the haptic interface "FEELEX"; indicating that a haptic interface which allows its users to interact with multiple points is preferable to those in which the user interacts with one point via a single finger or stylus. When a person's hand interacts with an object, the nerve endings in the hand transfer tactile and kinesthetic information about the object to the brain.

A vibrotactile system is one which stimulates the user by a mechanical vibration of the skin (Kaczmarek 1991). Chan et al. (Chan 2005) delivered haptic feedback during a study which tested the effectiveness of using vibrotactile sensation for communication between multiple users of a common software package. In this study subjects learned 7 different vibrational patterns, called "haptic icons," which were used to communicate the urgency of which other users needed the command of a shared artifact. The subjects of this study correctly identified the haptic icons 95% of the time while engaging in various levels of distraction based tasks intended to simulate multiple workloads. Under the most distractive task, where subjects were to assemble a digitized puzzle while listening for key words to be spoken, subjects detected a change in haptic icon in an average of 4.3 seconds. While vibrotactile feedback will support peripheral awareness of the

urgency in which multiple users wish to interact with a shared artifact (Chan 2005), more specific tests are required to implement a haptic icon-based sharing scheme in a "time- or safety-critical environment".

A number of devices have been developed for visually impaired users. Linvill and Bliss (Linvill 1966) developed a device which allowed blind subjects to read printed material while both Kaczmarek et al. (1994) and Nakashige et al. (2004) developed tactile arrays designed to display geometric entities to blind users. The device developed by Linvill and Bliss works by imaging each letter of a printed text onto an array of photocells which are connected to a tactile stimulator driver (Linvill 1966). The tactile stimulator drivers have a 12 x 8 array of vibrating pins attached to them which the subject can feel and interpret. Using this virotactile array blind users were able to read printed text at up to 30 words per minute. While this is significantly lower than the subjects' average Braille reading rate of 120 words per minute this study shows that through the use of vibrotactile stimulation, blind users are able to read normally printed text.

An electrotactile system, which stimulates the user by passing a local electric current through the skin, was developed by Kaczmarek (1991). Kaczmarek et al. developed an electrotactile array for the display of graphic information to visually impaired users (Kaczmarek 1994). Subjects were presented with 4 different sizes of 3 shapes for identification. The electrotactile array consisted of a 7 x 7 grid of 0.89 mm diameter electrodes which could be excited to produce the 12 combinations of shapes and sizes. Identical raised Braille-like patterns were embossed onto a Lexan polycarbonate sheet for

comparison. When a small current was conducted to each electrode, subjects were able to correctly identify the patterns approximately 75% of the time; obtaining higher accuracy for the larger shapes. However, the same subjects were able to correctly identify the same patterns in Braille-like embossed patterns approximately 95% of the time with a response time nearly 5 times faster than with the electrotactile array, indicating that raised bumps or pins are significantly easier to interpret than identical electrotactile patterns.

The tactile array created by Nakashige et al. consists of a base plate separated into a 10 x 10 grid of chambers which are each filled with 2.4 nano-liters of a low melting temperature metal (Nakashige 2004). A pin extends out of each chamber of metal, through a sealed cavity, and through a top plate which is accessible to the user. Applying heat to any given chamber melts the metal and allows the pin to move. Introducing compressed air into the sealed cavity between the molten metal and the top plate forces the pin to move up; similarly, if air is removed from the cavity the pin moves down. Each pin reaches a movable state approximately 5 seconds after the heating element is applied to the appropriate chamber (Nakashige 2004).

The specialized sensory organ in the human body that responds to mechanical stimuli such as tension, pressure, or displacement is the mechanoreceptor (Jost 1997), and the typical density is on the order of 200 receptors per square centimeter (Fearing 1997). To eliminate the need to create an array of actuators or stimulators with a density comparable to the human nervous system a skin is added over the stimulators, which provides a

"spatial low-pass filter" (Fearing 1997). The need for a tactile array to have a skin is amplified along with the scale of the array, therefore, most large scale tactile arrays have a skin above the actuator tips to create a surface that is smooth even with a lower density of actuators than is present in their finger-tip sized counterparts. FEELEX (Iwata 2001) is a 6 x 6 tactile array which uses DC motors coupled with screws to drive each actuator. The height of each actuator is calculated by measuring the revolutions of the motor with an optical encoder and force feedback is measured through a force sensor at the top of each actuator. FEELEX differs from many of the other haptic interfaces in that images are projected down onto the skin and the actuators are positioned to display the appropriate topology for the object that is being displayed. The use of servomotors limits FEELEX's force density as well as its range of motion, but the larger issue is that the servomotors consume precious real estate and significantly reduce FEELEX's ability to be scaled to a higher density array. Project Popup! uses a Shape Memory Alloy (SMA) as an actuator shaft and changes its length by applying current, which yields a response time of 0.8 seconds for the ascent, but 2 seconds for the decent of the rods (Nakatani 2003). In this system, like the FEELEX system, each actuator requires its own position measurement system. The position measurement used required each SMA actuator rod to be painted with stripes that are recognizable by a pair of photo reflectors, which read the discretized position of each actuator. While this approach works well for small numbers of actuators, a more scalable solution is desired (Nakatani 2003).

## 1.3 Fluidic-Based Tactile Arrays

Kikuuwe et al. developed a fluid-based tactile array for detecting small perturbations in surfaces (Kikuuwe 2004). This system consists of a small rectangular flexible container which is filled with a viscous fluid ($1x10^5$ $mm^2/s$). The bottom of the container has cantilevers protruding into the fluid so that when the container is moved over an irregularity in a smooth surface the bottom of the container flexes and strain gauges mounted on the cantilevers are used to quantify the magnitude of the surface irregularity. With this system, Kikuuwe et al. was able to detect a 0.09 mm thick piece of paper through a 5 mm thick sheet of rubber (Kikuuwe 2004).

A fluid that has the ability to translate from a liquid state to a pseudo-solid almost instantaneously upon the application of an electric field is an Electrorheological Fluid (ERF) (Taylor 1996). Taylor et al. designed a 5 x 5 tactile array which used an ERF for actuation and force feedback of the array. This system is composed of an array of aluminum bars which are covered by a thin layer of ERF and a conductive rubber skin. Connecting one of the aluminum bars to a high voltage source changes the fluid properties, including the viscosity, of the ERF in the vicinity of the excited aluminum bar. Therefore, a user palpating the skin will feel the difference in the excited region and will be able to infer information from the surface that would not have otherwise been available. Taylor and his co-workers developed this array for applications in virtual environments as a way to create the illusion that an object is present when, in reality, it is not. By exciting the array with 2.4 kV, it is possible to produce vertical and horizontal forces of approximately 1.8 N and .5 N respectively. While this array is clearly capable

of producing measurable forces on the surface it is not capable of physically deforming the skin to produce visually different surface geometries as the ERF layer is only 2.5 mm thick.

Melli-Huber et al. used an ERF in the design of a haptic vehicle control joystick (Melli-Huber 2003). In this design, a 2 degree of freedom joystick was created which has an actuator capable of producing torques on the joystick attached to each axis of rotation. Two actuator designs were tested; the first of which used concentric cylinders (CC) with an ERF filled gap between them and the second design used a shaft with multiple flat plates (FP) immersed in the ERF. The gap in the CC design was varied along with the number of plates and the gaps between them in the FP design. Tests were conducted to calculate both the static and dynamic torques by using various excitation voltages. A 300 mN-m dynamic torque and a 1000 mN-m static torque are created by applying approximately 1500 V and 2000 V respectively to the ERF in a 0.25 mm gap between the inner and outer cylinders in the CC design. Similarly, the FP design containing 4 flat plates with outer radii of 21 mm creates 300 mN-m of dynamic torque and 1000 mN-m of static torque by exciting the ERF with 2000 V in each case. Using these actuator designs Melli-Huber et al. were able to create a haptic joystick which is potentially capable of controlling many of the secondary controls within vehicle cockpits.

## 1.4 Digital Clay

In the present work, Digital Clay is a tactile array of linear fluidic actuators which provide distributed sensing and position control through the use of an embedded position

sensor. None of the tactile arrays or haptic sensors described in sections 1.1-1.3 provide the ability for the user to economically represent and interact with a desk-top sized topography through a remote software package. However, the Digital Clay project directly addresses these issues.

The Georgia Tech Digital Clay project focused on the development of two test beds. The first test bed (TB1), developed by Zhu (Zhu 2005), was comprised of a 5x5 tactile array of hydraulically actuated cylinders. It uses pressure sensors for force feedback and a capacitance based position sensor. While the capacitance based sensor is capable of accurately measuring positions down to 0.3 mm, it requires a wire to be attached to the piston rod, which decreases the robustness of the system as it can easily be broken or detached from the piston rod. This Digital Clay test bed (TB1) uses a combination of water and air as the working fluids. Water is used to move the cylinder up and a constant air pressure is used to move the cylinder down. Therefore, if the driving pressure is less than the air pressure in the cylinder the piston moves down and vise versa. While this design alleviates the need to create a tightly sealed upper cylinder cavity, it reduces the available forces of the piston and limits its downward velocity.

The second test bed (TB2), which is described in the present dissertation, focuses on a somewhat different approach, namely, the modularity of the design, maximum output force of an individual actuator, embedded position sensor design, and driving fluid selection.

Similar to TB1, TB2 presented here consists of multiple fluidic actuator cells which are attached to a base plate that is in fluidic communication with a high- and a low-pressure reservoir. However, in this work, each fluidic actuator contains its own driving electronics and can, therefore, be inserted into any location on the base plate, allowing for multiple actuator arrangements to be constructed with out the need to change or modify the base plate. The cylinders used to create the actuators are significantly larger than those used in TB1, which allow for greater output forces by each individual actuator. The version of Digital Clay that is presented here (TB2) uses a Variable Core Transformer (VCT) in place of the capacitance measurement system used in TB1 to create a more robust sensor. The VCT is more robust than the capacitance sensor used in TB1 because the VCT does not require a physical connection between the piston rod and the sensor electronics. Finally, silicone oil is used for the driving fluid in this work in stead of the water and air combination used in TB1. The notable characteristics of this particular fluid are its chemical compatibility with the mechanical elements of the system, its enhanced lubrication qualities, and its high permeability, which enhances the performance of the VCT.

Both of the Digital Clay test beds, developed in parallel, can be interfaced through a network, or internet connection running their respective host software packages. The capacitance based position sensor created for TB1 as well as the variable core transformer position measurement system created here are simple and economic to build and manufacture.

A single actuator is tested and characterized for implementation into a 5x5 array of actuators. The design and implementation of the experimental apparatus and measurement techniques needed to drive and characterize a single fluidic actuator cell are presented in Chapter 2 along with the appropriate calibration techniques. Chapter 3 outlines the Variable Core Transformer used for embedded position measurement, its implementation, and its characterization. Chapter 4 describes the closed-loop controller used for the autonomous control of a single actuator and the methods used to test the closed-loop controller. Also included in Chapter 4 are the actuator piston velocity, acceleration, and friction force calculations.

# CHAPTER 2

# EXPERIMENTAL APPARATUS AND TECHNIQUES

As discussed in Chapter 1, Digital Clay is comprised of an array of interactively activated fluidic actuators which provide both distributed sensing and actuation functionality. Each actuator is composed of a hydraulically-driven piston whose position is sensed by an embedded variable core transformer which is discussed in detail in Chapter 3. The actuators are integrated with computer controlled valves and an underlying base plate that is in fluidic communication with high and low-pressure fluid reservoirs. However, each actuator utilizes a modular design and is completely independent of the other actuators that are connected to the base plate. The fluidic loop is discussed in section 2.1.

## 2.1 Fluid Loop

The operation of the actuator is shown schematically in Figure 1. When the piston is in motion, fluid flows from the high pressure reservoir, through the fluidic actuator, and into the low-pressure return tank. From the return tank the fluid is pumped through a filter and a check valve back into the high pressure reservoir. The system components of Digital Clay are described in detail in section 2.2. Also described below are the measurement techniques that are used in the present work and their associated hardware. As seen in Figure 1, the primary components of the fluid loop are the fluidic actuator, the high – and low – pressure fluid reservoirs, the system pumps, a regulated pressurized air source, and the associated plumbing.

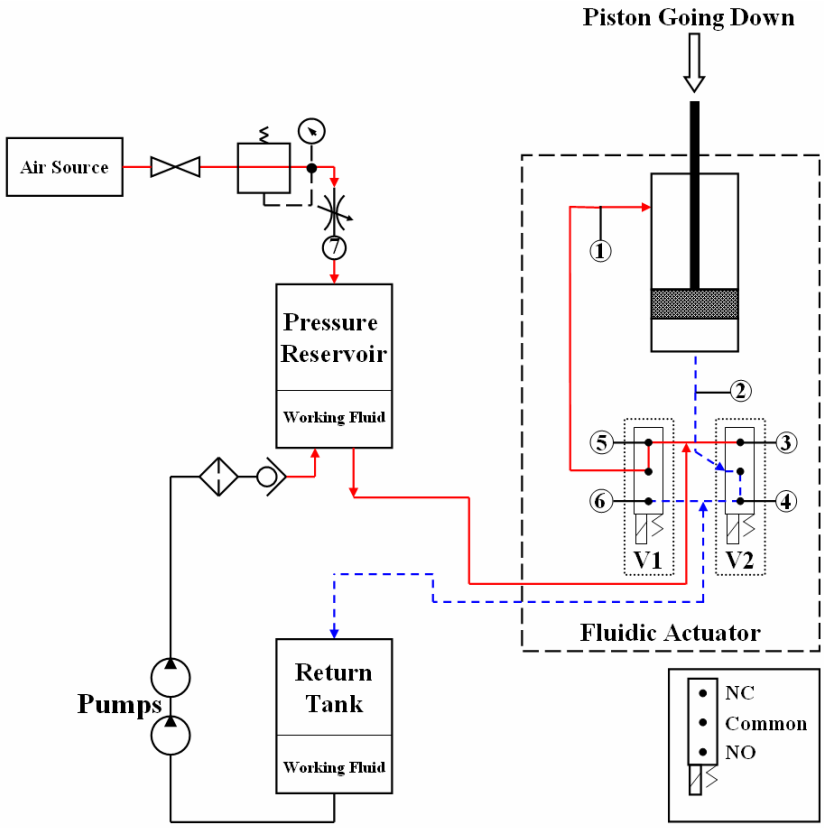


***Figure 1:*** *Diagram of Fluid System showing high (-) and low (--) pressure lines*

The piston motion is controlled by two three port solenoid valves (V1 and V2) (Lee Company) which are shown schematically in Figure 1 enclosed in dotted boxes and labeled. The ports of a three-port valve are the normally closed (NC) port, the common port, and the normally open (NO) port. As seen in Figure 1, the pressurized fluid line is connected to the NC ports of V1 and V2 while the low-pressure fluid line is connected to the NO ports of V1 and V2. The common port of V1 is connected to the upper cavity of the cylinder and the common port of V2 is connected to the lower cavity of the piston. When either V1 or V2 is closed, it restricts fluid from flowing through the NC port, but allows fluid flow between the common port and the NO port. Similarly, when either valve is opened, it connects the NC port to the common port and allows fluid to flow between the NC port and the common port, while restricting fluid from flowing through

the NO port. Therefore, when either valve is closed, the NO port is connected to the common port.

Since the piston can be actuated in either direction, both the bottom and the top cavity of the piston are filled with the working fluid at all times. In order to move the piston down, fluid must move from the pressurized reservoir, through V1, and into the upper cylinder cavity. This pressurized fluid forces the piston down while concomitantly pushing the fluid in the lower cylinder cavity through V2 and into the return tank. Both of these tasks are accomplished by opening V1. Valve V2 does not have to be open to allow fluid to flow through it as the piston moves down because the common port of V2 is connected to the lower cylinder cavity and the valve is closed, which allows fluid to flow from the common port through the NO port and into the return tank as described above. Similarly, to move the piston up, pressurized fluid must enter into the lower cavity of the cylinder and push the piston up while the fluid that is above the piston is simultaneously allowed to exit the upper cylinder cavity and flow into the return tank; both of which are accomplished by opening V2.

Two small gear pumps (connected in series) are used to pump the fluid from the return tank back into the pressurized reservoir (30 psi) with sufficient head. Placing the pumps under the low pressure return tank provides continuous flow and alleviates the problems with pumping air bubbles through the system. A liquid level sensor within the low pressure return tank is used to turn the pumps on and off to maintain fluid between two

desired levels in the return tank. A 40 μm filter between the second pump and the pressurized reservoir is used to remove particles from the working fluid.

## 2.2 Fluidic Actuator

The fluidic actuator, which is nominally 125 mm tall (30 mm travel), shown in Figure 2, is comprised of several components: a steel shaft, Teflon top and bottom seals, an o-ring injection sleeve, a glass cylinder, a graphite piston head, and a housing made out of stereolithography (SLA). The function of the SLA housing is to provide a modular element into which all of the above items can be inserted. The exterior of the SLA housing provides the appropriate connections and mounting surfaces for the valves and the high and low-pressure lines, which connect the actuator to the high and low-pressure fluid reservoirs, as shown in Figure 1. The interior of the SLA housing contains the fluid channels which connect the NC and NO valve ports to the high and low-pressure lines respectively as well as the fluid channels which connect the common valve ports to the upper and lower cylinder cavities. The glass cylinder has a hole that is approximately 2 mm in diameter drilled into its side that is nominally 17 mm from the top of the cylinder. It is through this hole that fluid passes into and out of the upper cylinder cavity. As seen in Figure 2, the graphite piston head is attached to the end of the steel actuator shaft and is inserted into the glass cylinder between the top and bottom Teflon seals, which are also inserted into the glass cylinder. The above assembly is wrapped with magnet wire to form the VCT, which is discussed in detail in Chapter 3, and inserted into a hole along the centerline of the SLA housing which is approximately 76 mm deep.

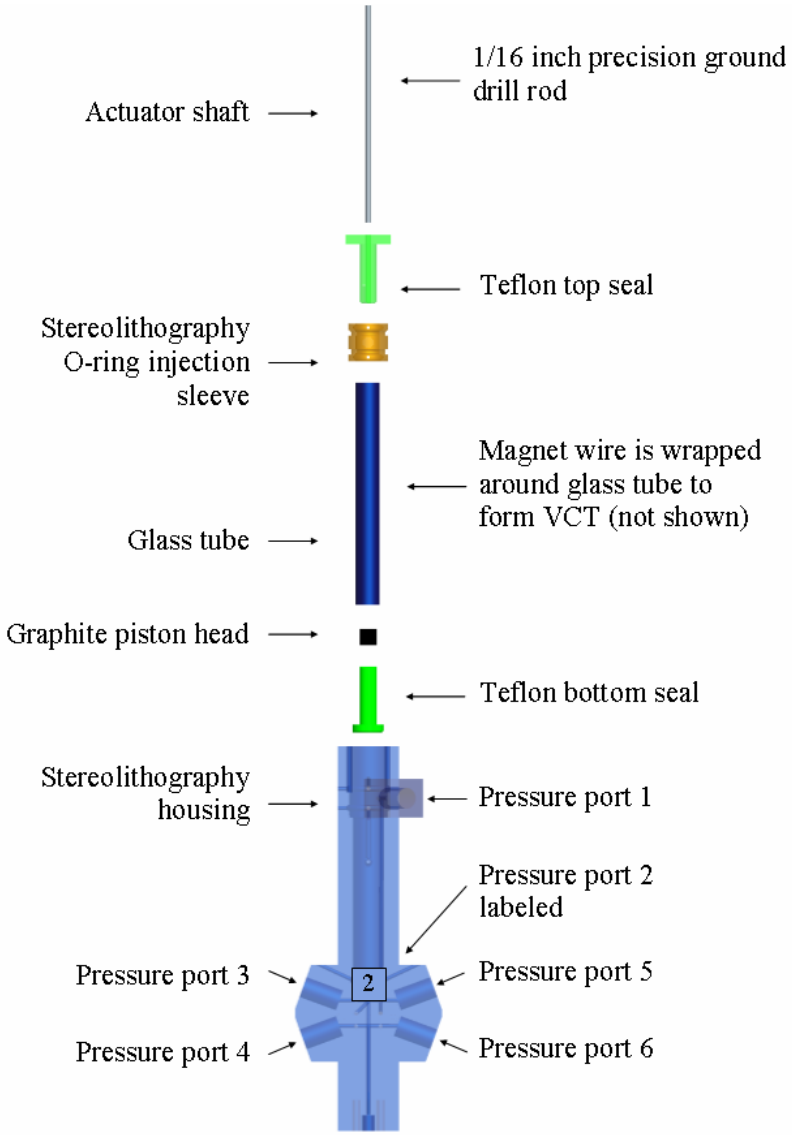


***Figure 2:*** *Exploded CAD model of Fluidic Actuator (Valves Not Shown)*

However, there is a gap in the radial direction between the glass cylinder and the SLA housing when the glass cylinder is inserted into the SLA housing. An SLA O-ring injection sleeve, shown in Figure 2, slides over the glass cylinder and is used to fill the gap between the glass cylinder and the SLA housing in order to create a sealed channel through which fluid can flow into and out of the upper cylinder cavity. The O-ring injection sleeve has a hole in its side that is approximately 4 mm in diameter which is

aligned with the 2 mm diameter hole in the glass cylinder. These holes are aligned with the channel which connects the common port of V1 to the upper cylinder cavity. Therefore, when the O-ring injection sleeve is installed, fluid is allowed to move from V1, through the channel in the SLA housing, through the sealed O-ring injection sleeve, through the hole in the glass cylinder, and into the upper cavity of the cylinder. The Teflon top seal bolts into the top of the SLA housing to further secure the assembly into the SLA housing. As seen in Figure 2, pressure ports 3 and 4 are symmetric to ports 5 and 6 about the centerline of the SLA housing, pressure port 2 is centered between ports 3 and 5 and is orthogonal to the axis of motion of the piston, and pressure port 1 is located towards the top of the piston where the working fluid enters and exits the upper cavity of the cylinder.

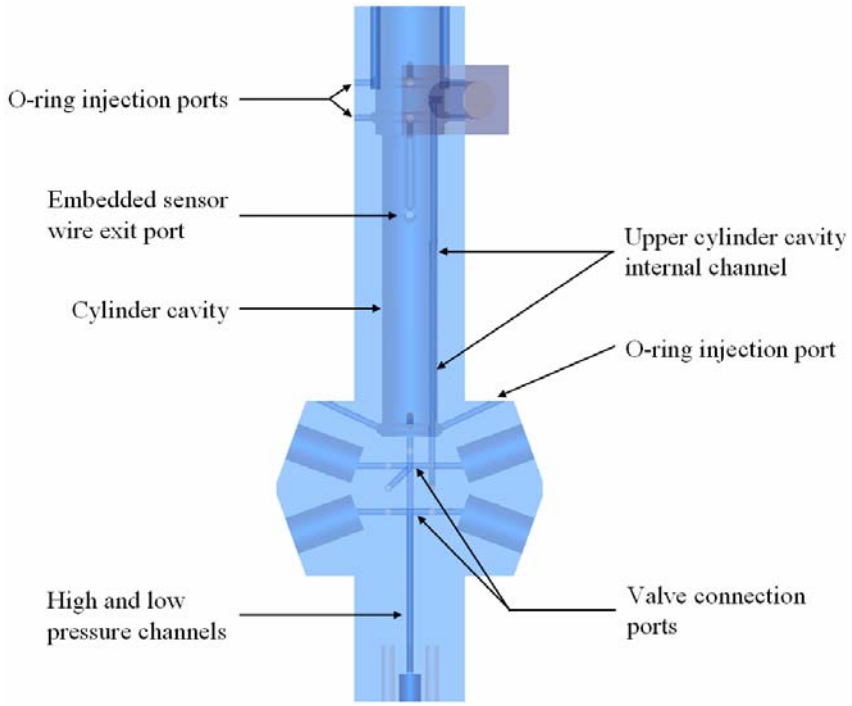


***Figure 3:*** *CAD Model of stereolithographed actuator housing*

Figure 3 shows a CAD model of the stereolithographed actuator housing. This fabrication approach enables the construction of the actuator housing and the intricate internal channels and is particularly useful for prototyping purposes. The disadvantages of using SLA are that it is difficult to maintain tight tolerances, and it is not as dimensionally stable as metal or plastic. Therefore, segments of the actuator housing which require high tolerance, such as the diameter of the cylinder, cavity are reamed to ensure a tight fit.

The material selections of graphite and glass for the respective piston head and cylinder are preferable because of their mutually low static and kinetic coefficients of friction as well as for their availability. Drill rod is used for the steel shaft because of its high dimensional stability and surface finish.

One area of focus is the design of the seal that prevents fluid from leaking out around the reciprocating piston at the top of the actuator. Originally, a double lipped O-ring that fit tightly around the steel shaft was used. Although this method of sealing the reciprocating shaft was effective in preventing the leakage of fluid, it exerted excessive friction force on the steel actuator shaft. The solution was to fabricate a Teflon seal to minimize the static and kinetic coefficients of friction with the steel shaft. This sealing approach allows the piston to be driven with lower pressures than with the previously mentioned O-ring design. A Teflon seal is also used to prevent fluid from leaking out of the bottom of the glass cylinder into the SLA housing.

## 2.3 Measurement Techniques

Three pressure transducers are used for the acquisition of the pressure data presented in this work. Two miniature pressure transducers (XPM5 343 and XPM5 344, GS Sensors) are used and are referenced hereafter as T1 and T2 while the third transducer (PMP 4010, Druck) is referenced hereafter as T3. All of the above pressure transducers have ranges of 0-30 psi and resolutions of 0.015 psi. Sensors T1 and T2 have accuracies of 0.25% full scale, and T3 has an accuracy of 0.08% full scale. As shown in Figure 1 there are seven numbered pressure ports which are located on the high and low-pressure sides of each valve, the channels leading into both the upper and lower cavities of the cylinder, and the supply line to the pressurized reservoir. Sensors T1 and T2 are used to monitor the pressures in the actuator (pressure ports 1-6) while T3 is used to measure the pressure of the pressurized reservoir (pressure port 7).

### *2.3.1 Pressure Measurements*

Ports 3 and 5 in Figure 1 are connected to the high pressure channels of the actuator and ports 4 and 6 are connected to low-pressure channels. However, ports 1 and 2 are connected to either high or low-pressure depending on the actuation direction of the piston. Air that is trapped in the pressure ports when the pressure transducers are removed is purged by slight pressurization of the system; the working fluid is collected and funneled back into a return tank. The fluidic actuator is constructed of translucent SLA which allows for a visual inspection of this method.

Table 1 details 5 combinations of T1 and T2 measurements that are needed to calculate the pressure difference across each of the system components.

***Table 1:*** *Transducer Case Numbering Scheme*

| Case | Ports | | Pressure Drop Across | Piston Motion |
|---|---|---|---|---|
| 1 | 1 | 2 | Piston | Up and Down |
| 2 | 1 | 5 | V1/ HP Res to FA | Down |
| 3 | 1 | 6 | V1/ FA to LP Res | Up |
| 4 | 2 | 3 | V2/ HP Res to FA | Up |
| 5 | 2 | 4 | V2/ FA to LP Res | Down |

The pressure difference across the piston as it moves either up or down is measured across ports 1 and 2 (case 1 Table 1). The pressure difference across V1 and its associated channels as the piston is moving down as well as the pressure difference from the NC port of V1 to the high-pressure reservoir, along with data from T3, are measured across ports 1 and 5 (case 2 Table 1). The pressure difference across V1 and its associated channels as the piston is moving up as well as the pressure difference from the NO port of V1 to the low pressure reservoir are measured across ports 1 and 6 (case 3 Table 1). The pressure difference across V2 and its associated channels as the piston moves up is measured across ports 2 and 3 and, along with data from T3, provides the pressure difference from the high pressure reservoir to the NC port of V2 (case 4 Table 1). The pressure difference across V2 as the piston is moving down as well as the pressure difference from the NO port of V2 to the low-pressure reservoir is measured across ports 2 and 4 (case 5 Table 1). The pressure data are digitized at 1 KHz by an A/D board (AT-MIO-16-E1) that is controlled by LabView software. All data presented in this work was taken with the above hardware and interfacing software. The pressure data are discussed in Chapter 4.

### *2.3.2 Position Measurements*

An optical displacement measurement system (optoNCDT 1605, Micro-Epsilon) was used to verify the position measurements obtained from the variable core transformer (VCT). The optical displacement measurement system functions on the principle of triangulation measurement whereby a laser beam is focused on the target and the diffuse reflection is focused on a position sensor as shown in Figure 4. The optical measurement system outputs a voltage that is linearly proportional to the measured distance between the measurement device and the target for the measurable range of the device (100 mm). Calibration data for the optical displacement measurement system and the VCT are shown in section 2.4.

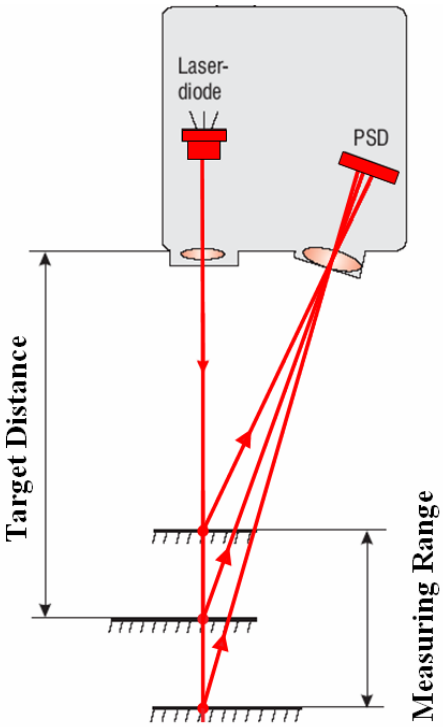


***Figure 4:*** *Optical Displacement Measurement System Operation Diagram (Courtesy of Micro-Epsilon)*

An optical measurement pad is attached to the top of the piston rod to provide a measuring surface for the optical displacement measurement system. Position data was recorded from the optical displacement measurement system and the VCT for all of the cases that are described in section 2.3.1 and is presented in Chapter 3 along with a description of the design and operation of the VCT. The VCT is constructed by wrapping magnet wire around the glass cylinder, which is inserted into the actuator.

In order to resolve the forces that are exerted on the piston it was necessary to independently measure the friction force between the steel actuator shaft and the Teflon top seal. The friction force test stand, shown in Figure 5, was constructed to facilitate the isolation of the friction force acting on the shaft as a result of the Teflon top seal.

When the Teflon top seal is attached to the actuator it is inserted into the glass cylinder as described in section 2.2. The diameter of the Teflon top seal is approximately 0.03 mm larger than the inside diameter of the glass cylinder. Therefore, when the Teflon top seal is inserted into the glass cylinder a compressive force is exerted on the Teflon top seal by the glass cylinder. This compressive force acts on the steel actuator shaft which is inserted into a hole in the center of the Teflon top seal. The O-ring injection sleeve is pressed onto the glass tube, which adds to the compressive force acting on the steel actuator shaft.

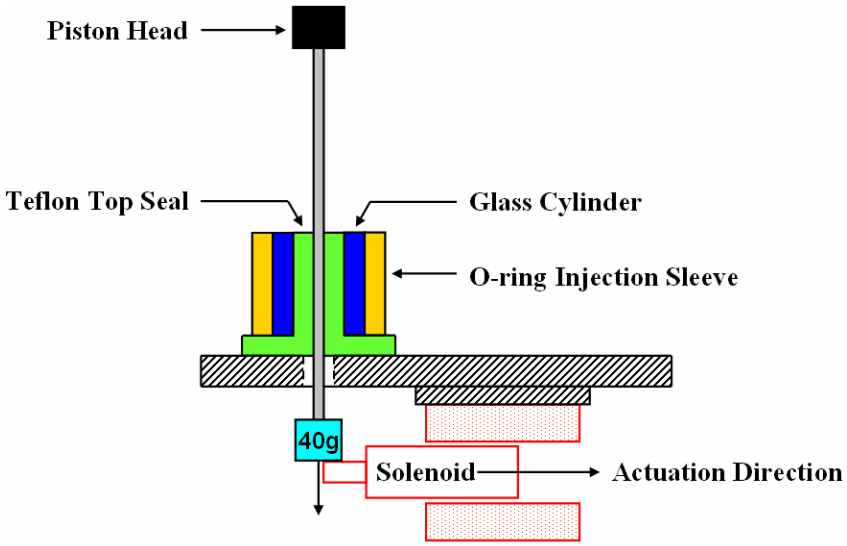


***Figure 5:*** *Friction Force Test Stand*

The friction force test stand, shown in Figure 5, consists of a rigid base, a solenoid core and associated solenoid coil, a 40 gram mass, steel actuator shaft, Teflon top seal, glass cylinder, O-ring injection sleeve, and the piston head. The solenoid shown in Figure 5 is actuated with a TTL signal from the data acquisition computer and the interface of the Teflon top seal and the steel actuator shaft is kept well lubricated with the working fluid. When the solenoid coil is energized the solenoid core moves to the right and the 40 gram mass pulls the steel shaft down through the Teflon top seal. A 40 gram mass was used because it was experimentally determined to be large enough to immediately move the actuator shaft upon excitation of the solenoid, but no so large that damage was caused to the piston head upon termination of motion. In order to accurately measure the friction force exerted on the steel actuator shaft by the Teflon top seal a portion of the glass tube and O-ring injection sleeve were included in the friction force test stand as seen in Figure 5.

The optical displacement measurement system is placed above the piston head and used to sample the position of the piston head at 100 KHz for 0.11 seconds as the piston is pulled downward by the 40 g mass. The position data from this test is used to calculate the friction force acting on the steel actuator shaft and is presented along with the associated friction force calculations in Chapter 4.

## 2.4 Calibration

The pressure transducers, the optical displacement measurement system, and the variable core transformer (VCT) were calibrated periodically during the course of the measurements as described in this section.

### *2.4.1 Pressure Calibration*

A calibration station was constructed in order to calibrate the three pressure transducers simultaneously using a test gauge and pressure regulator. The test gauge (Q-8638, Omega Engineering Inc) has an accuracy of 0.25% full scale, resolution of 0.2 psi, and a range of – 762 mm Hg to 30 psi. During calibration, pressure data are sampled at 1 KHz for 10 seconds from T1, T2, and T3 in 5 psi increments and recorded. The calibration curves for the three pressure transducers are shown in Figure 6. Calibration is conducted by changing the supply pressure until the test gauge reads a specified value (0-25 psi in 5 psi increments) and measuring the respective output voltages of T1, T2, and T3. The values shown in Figure 7 are obtained by calculating the difference between the pressure read on the test gauge and the pressure measured from the three transducers. These differences are the bias errors of the transducers.

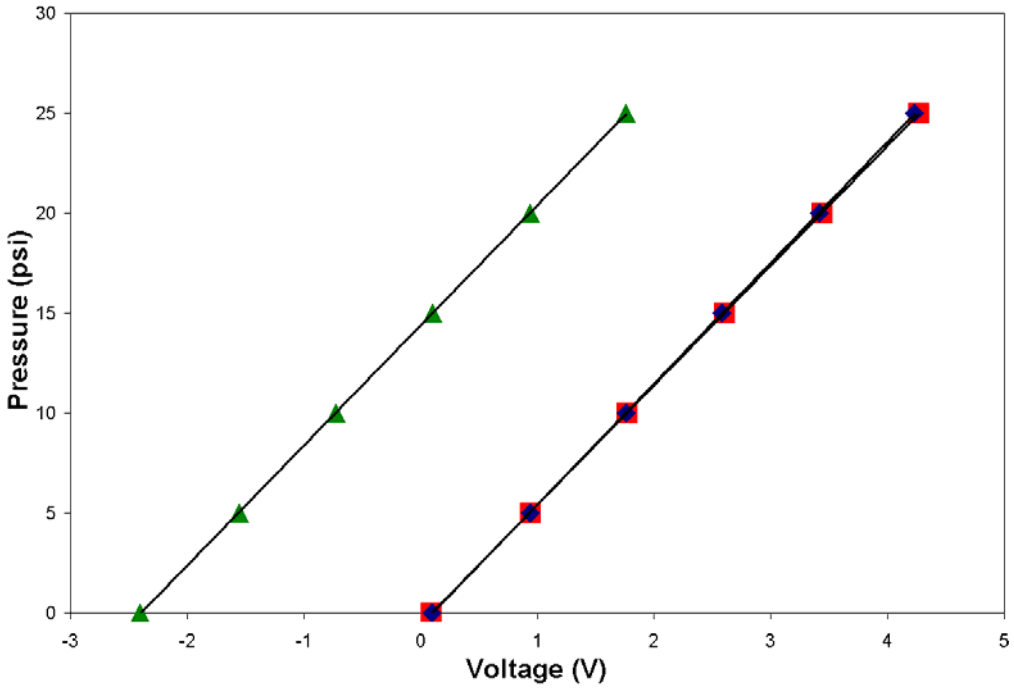


***Figure 6:*** *Transducer Calibration Curves for T1(■), T2(♦), and T3(▲)*

The calibration curves for T1, T2, and T3 are shown in Equations 1-3 respectively

$$T1: \quad y = 6.02x - 0.43 \qquad (1)$$
$$R^2 = 1$$
$$T2: \quad y = 6.05x - 0.79 \qquad (2)$$
$$R^2 = 1$$
$$T3: \quad y = 6.01x + 14.27 \qquad (3)$$
$$R^2 = 1$$

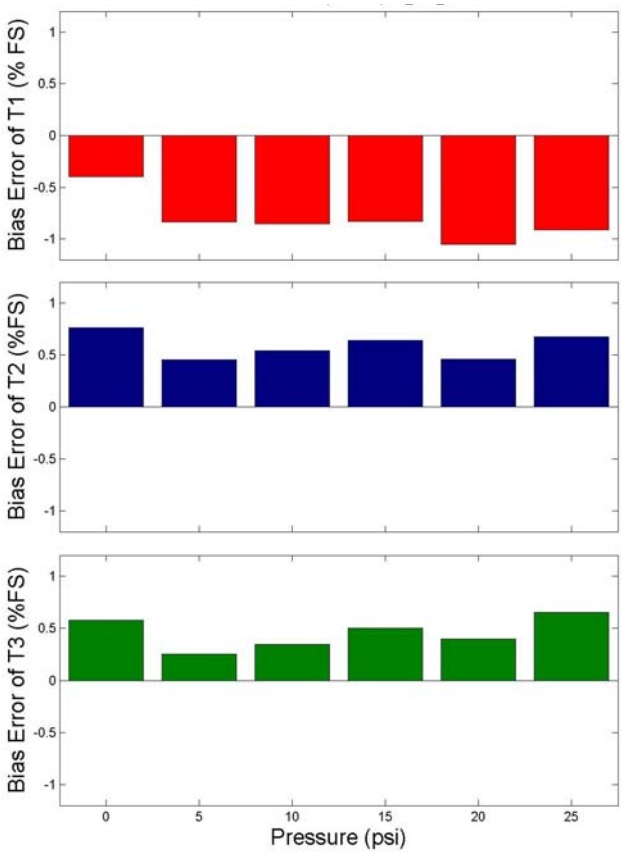


***Figure 7:*** *Bias Error of T1 (Top), T2 (Middle), and T3 (Bottom)*

### *2.4.2 Position Calibration*

A position calibration station was constructed and is shown in Figure 8. The position calibration station was constructed to calibrate the optical displacement measurement system and the variable core transformer concomitantly. The calibration station consists of an optical stand, the optical displacement measurement system (0.008 mm resolution), the actuator, and a traverse outfitted with a micrometer (63P 50305, The L. Sarrett Co). The micrometer barrel has a nominal range of 50 mm and a resolution of 0.0254 mm. The optical displacement measurement system is positioned on the optical stand so that the incident beam is centered on the top of the measuring pad of the actuator and the range of motion of the piston (30 mm) is within the measurable range of the optical

displacement measurement system (100 mm) and the movable range of the traverse (50 mm).

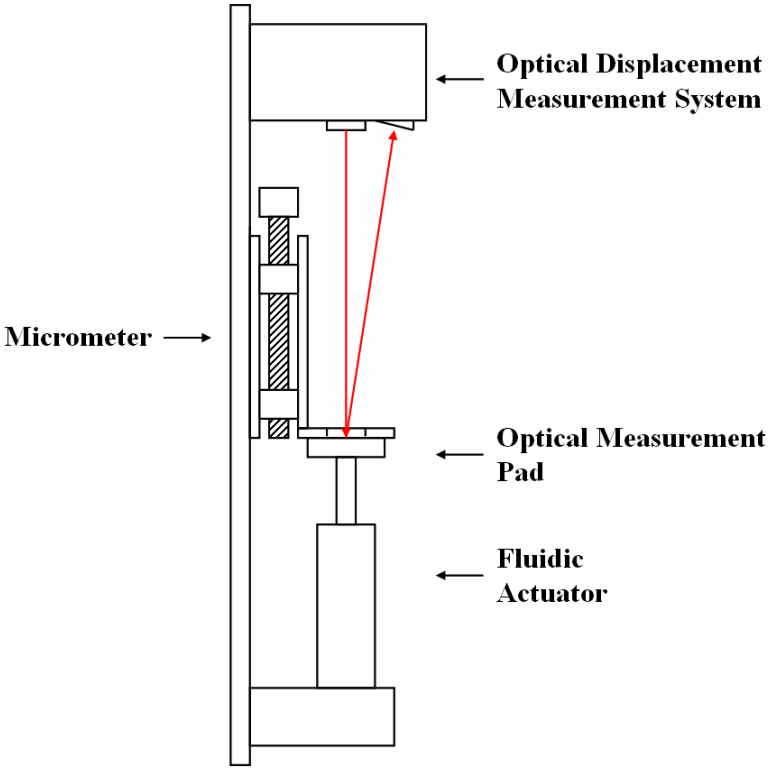


***Figure 8:*** *Position Calibration Station*

The calibration curves for the optical displacement measurement system and the variable core transformer are obtained by moving the piston to its fully retracted position and setting that location as reference. The traverse is then moved through the range of piston motion in 0.635 mm (one turn of the micrometer) increments. The output of the optical displacement measurement system and the variable core transformer are sampled at 1 KHz for 10 seconds at each location and recorded. The calibration curves for the optical displacement measurement system and the variable core transformer as obtained from the position calibration station are shown in Figure 9.

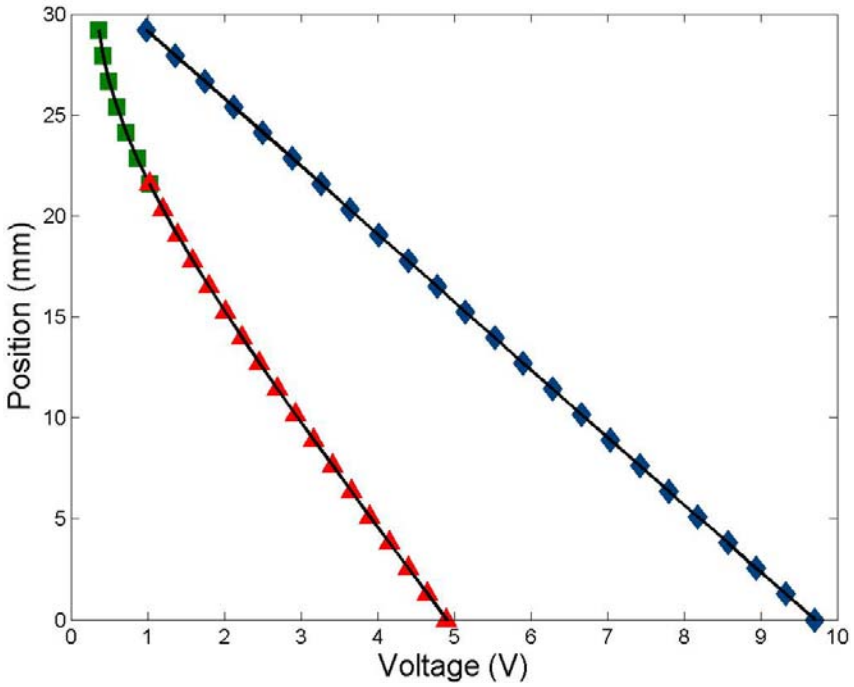


***Figure 9:*** *Laser(♦) and variable core transformer(■, ▲) curves*

Least squares polynomial fits are shown in Figure 9 for the calibrated optical displacement measurement system and the variable core transformer data. The calibration curves for the variable core transformer are Equations 1 and 2 and the calibration curve for the optical displacement measurement system is Equation 3. The respective goodness of fit parameters are also given.

$$y = -19.652x3 + 50.192x2 - 50.53x + 41.787 \quad (4)$$
$$R^2 = 1$$
$$y = -0.0711x3 + 0.8426x2 - 8.4182x + 29.351 \quad (5)$$
$$R^2 = 1$$
$$y = -3.351x + 32.505 \quad (6)$$
$$R^2 = 1$$

Figure 10 shows the position measured from the micrometer along with the calibrated optical displacement measurement system data and the calibrated variable core transformer data as obtained from the Equations 4-6 respectively.

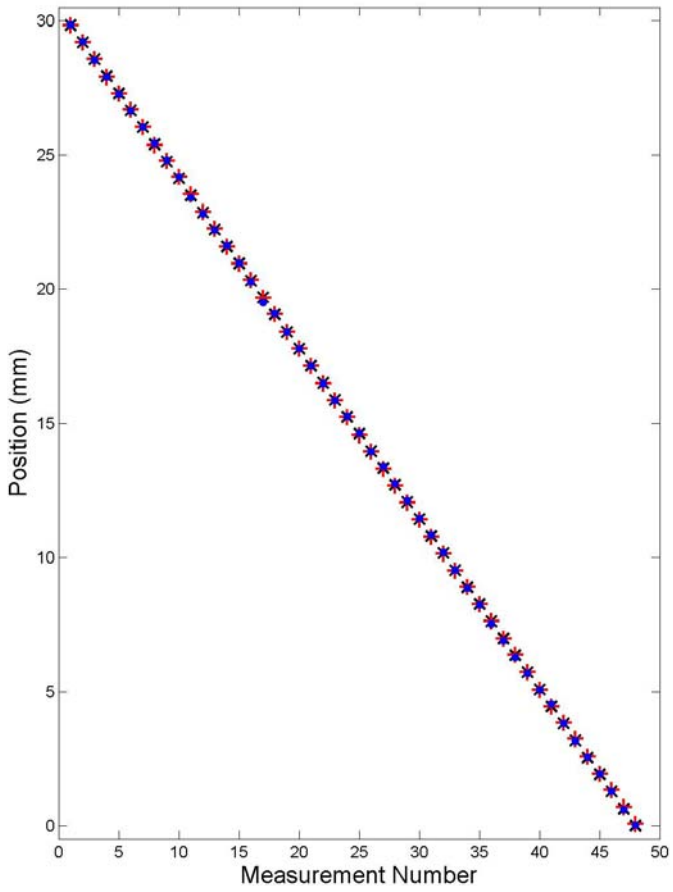


***Figure 10:*** *Micrometer Position (×), optical displacement measurement system position (+), variable core transformer Position (•)*

The bias errors of the VCT and the optical displacement measurement system are obtained by subtracting the respective calibrated position measurements from the known position of the micrometer (Equation 7) where $P_T$ is the position of the micrometer and $P_S$ is the position measured by either the VCT or the optical displacement measurement system.

$$e_B = P_T - P_S \tag{7}$$

The variation of the bias errors of the optical displacement measurement system and the VCT with piston position are shown in Figure 11. The largest bias error of the VCT is -0.17 mm, which is approximately 0.6 % full scale. While largest bias error measured

from the optical displacement measurement system is 0.08 mm, which corresponds to approximately 0.3 % full scale.

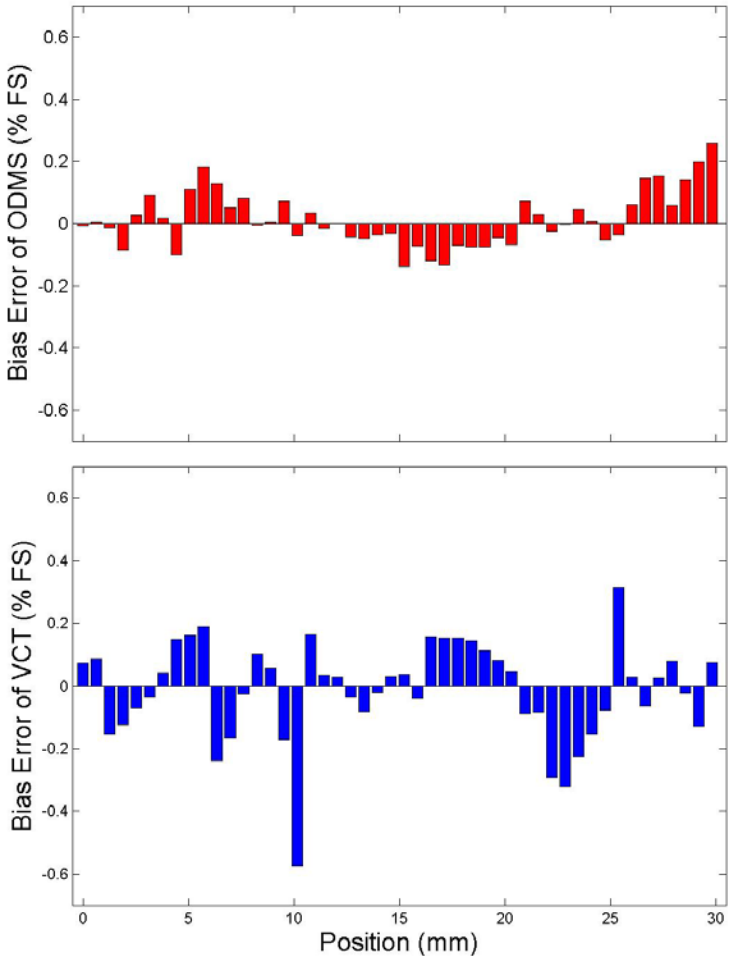


***Figure 11:*** *Bias Error of ODMS and VCT*

The average bias error of the optical displacement measurement system is 0.014% full scale with a standard deviation of 0.09 % full scale while the average bias error of the variable core transformer is 0.014 % full scale with a standard deviation of 0.16% full scale. The variable core transformer is discussed in more detail in Chapter 3.

# CHAPTER 3

# CHARACTERIZATION OF VCT FOR POSITION MEASUREMENT

A Variable Core Transformer (VCT) was designed, constructed, and integrated with the fluidic actuator for highly resolved position sensing. This chapter details the design and implementation of the VCT by focusing its principle of operation and practical implementation. As discussed below, the variable core transformer is developed based on a Linear Variable Differential Transformer (LVDT). The present variable core transformer has two overlapping coils where the excitation of the primary coil results in a magnetic field which induces a current in the secondary coil. The voltage induced in the secondary coil is controlled by the ratio of turns of the primary to the secondary coils. A full characterization of the VCT is presented in section 3.3, including sensitivity and resolution analysis, repeatability, and drift calculations as a function of piston position.

## 3.1 Theory of Operation

When an electric current flows through a wire coil a magnetic field is established. The magnetic flux $\Phi_B$ through a differential area $d\vec{A}$ in a magnetic field $\vec{B}$ is

$$d\Phi_B = \vec{B} \bullet d\vec{A} = BdA\cos\theta \tag{8}$$

(Young 1996) where $\theta$ is the angle between the magnetic field $\vec{B}$ and differential area dA (Figure 12).

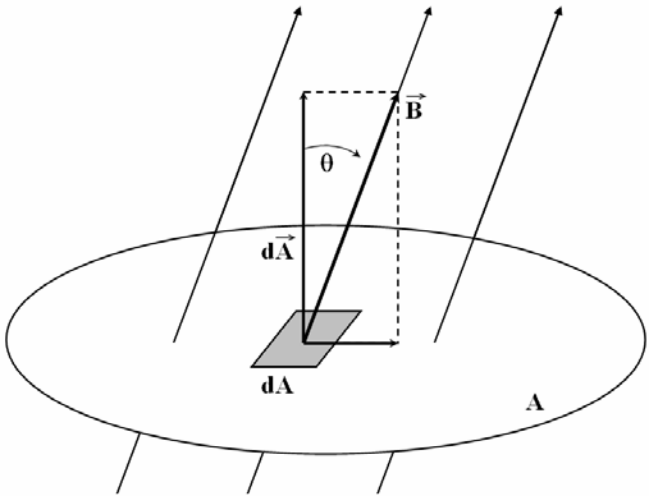


***Figure 12:*** *Magnetic Flux Through Differential Area dA*

The total magnetic flux through area dA is given by integrating the magnetic flux over area A.

$$\Phi_B = \int \vec{B} \bullet d\vec{A} = \int BdA\cos\theta \tag{9}$$

If the magnetic field is uniform and orthogonal to area A then the magnetic flux through A.

$$\Phi_B = BA \tag{10}$$

Based on Faraday's induction law, if the area A, (Figure 12), is bounded by a conductor, then a changing magnetic flux through A induces an electromotive force through the bounding wire (Rizzoni 2000). One way to increase the induced voltage in the wire is to use a coil of wire (Figure 13) having N turns so that the induced emf, $\varepsilon$, in the coil is

$$\varepsilon = N\frac{d\Phi_B}{dt} \tag{11}$$

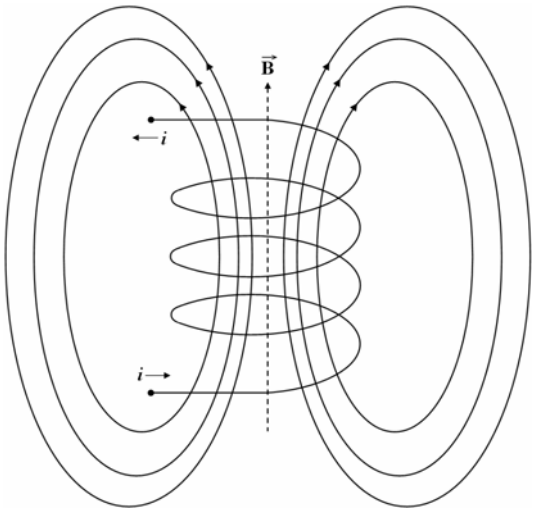


***Figure 13:*** *Induced emf in Coil*

(Young 1996). In the absence of a time varying magnetic flux there is no induced voltage in the coil but an alternating current generates an alternating magnetic flux.

In a transformer excitation of the primary coil with an alternating (AC) voltage, creates a time varying magnetic flux through the magnetic core and induces a current in the secondary coil. The induced voltage in the secondary coil is

$$\varepsilon = \frac{n_2 \mu_0 \mu_r A}{l} \frac{di}{dt} \tag{12}$$

where $n_2$ is the number of turns in the secondary coil, $\mu_0$ is the permeability of free space, $\mu_r$ is the relative permeability of the core, $l$ is the length of the coil, A is the cross sectional area of the core, θ is the angle between the magnetic field B and the cross sectional area, as defined in Figure 12, and $i$ is the current in the primary coil. In Equation 12, it is assumed that the windings of the transformer coils about the magnetic form are sufficiently close so that the induced voltage is not affected by the spacing of the wire on the form (Welsby 1950). Therefore, fixing the length, $l$, of the transformer and

increasing the diameter of the wire used in the secondary coil effectively decreases the number of turns in the secondary coil, and decreases the induced voltage in the secondary coil. Equation 12 also shows that increasing the diameter of the transformer core increases the cross sectional area A and the induced voltage in the secondary coil. The induced voltage in the secondary coil ($V_2$) is proportional to the excitation voltage of the primary coil ($V_1$) by the turns ratio of the transformer (N) which is the ratio of the number of turns in the secondary coil to the number of turns in the primary coil.

$$\tilde{V}_2 = N\tilde{V}_1 \tag{13}$$

## 3.2 System Implementation

A Linear Variable Differential Transformer (LVDT) is a robust position measurement device which works on the principle of magnetic flux coupling. LVDTs consist of an arrangement of primary and secondary coils, inside of which is a movable magnetic core (Figure 14). The primary and secondary coils are wound such that movement of the magnetic core induces a voltage in the secondary coils which varies linearly with displacement. Attached to the magnetic core is a non-magnetic rod, which is mechanically coupled to the variable of interest for position measurement. Linear variable differential transformers only have one moving part (magnetic core) and are typically designed in a way which isolates the coils from their surroundings, allowing them to function well in hostile environments.

In a Linear Variable Differential Transformer (LVDT) the voltage from a primary coil induces a voltage into the secondary coils as described in section 3.1. Figure 14 shows

the coil arrangement of a typical LVDT where positive and negative displacements of the core are measured with respect to the core's center position.

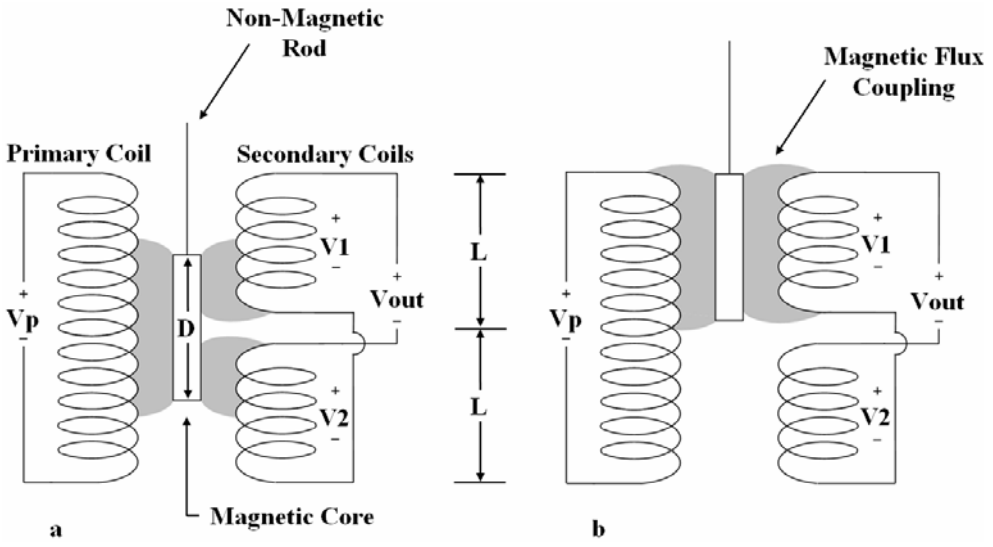


***Figure 14:*** *LVDT Schematic Showing Flux Coupling*

The time varying magnetic field created by the excitation of the primary coil is greater in the region surrounding the magnetic core than it is in regions which are not in close proximity to the movable magnetic core. Assuming that the secondary coils are identical, when the magnetic core is in its center position, as shown in Figure 14a, the changing magnetic flux of the primary coil engages the same number of turns in the upper secondary coil as it does in the lower secondary coil, which induces voltages of the same magnitude in the upper ($V_1$) and lower ($V_2$) secondary coils. However, the coils are connected such that the output voltage, $V_{out}$, is the subtraction of $V_2$ from $V_1$, which gives an output voltage of zero. If the magnetic core is moved upward with respect to the center position by moving the non-magnetic coupling rod, as shown in Figure 14b, then the magnetic flux from the primary coil engages more windings on the upper secondary

coil and the induced voltage ($V_1$) in the upper secondary coil increases with "positive" core displacement. Similarly, $V_2$ increases with "negative" core displacement.

As shown in Figure 14, the LVDT output is zero when the magnetic core is in the center of its range of motion only if the "upper" and "lower" secondary coils are identical. Once the core is in a position where the magnetic flux is coupled completely with one of the secondary coils (Figure 14b), any additional motion of the core does not yield a further change in voltage because the same number of windings are being added as are being subtracted. This means that for a typical LVDT the measurable range of the sensor is limited by the length of the core and the distance between the upper and lower secondary coils. The upper bound for the measurable range of an LVDT is limited by the geometry of the device. Also labeled in Figure 14 are the lengths of the upper and lower coils (L) as well as the length of the magnetic core (D). The length of the magnetic core (D) is necessarily larger than L so that the core is always engaging both of the secondary coils. Therefore, the upper bound of the motion of the core is slightly less than 2D. For many applications the size of the sensor is inconsequential, however, for small systems where space is critical, traditional LVDTs may be harder to implement.

The Variable Core Transformer (VCT) operates on the same magnetic flux coupling principle as the LVDT, but has a different geometry which is more suitable for use in compact applications such as the fluidic actuator. The design of the VCT takes advantage of the fact that the sensor does not make physical contact with the piston and therefore, does not contribute additional friction forces to the piston. Because there is no

mechanical interaction between the VCT and the piston rod there is no wear on the VCT, which gives the VCT long service life.

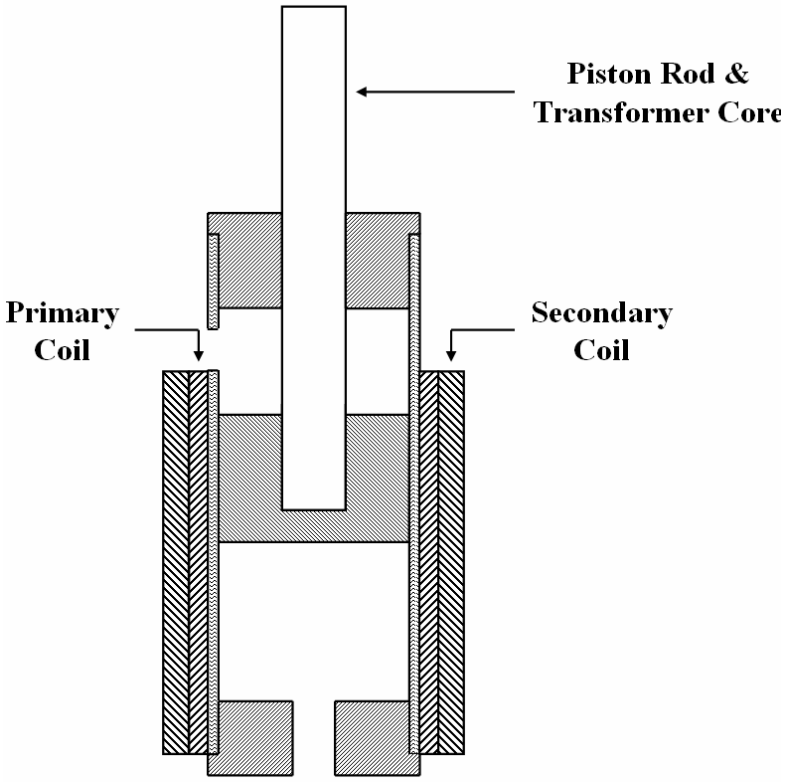


***Figure 15:*** *Variable Core Transformer Implementation*

Figure 15 shows the piston, cylinder, Teflon seals, and the windings needed to make the VCT operate as a piston and a position measurement system. The VCT uses overlapping primary and secondary coils. With this design, the induced voltage in the secondary coil is continuously increasing as the transformer core, or piston rod, moves into the cylinder cavity. The salient characteristics of the steel core are its availability, surface characteristics, and mechanical properties. Although a ferromagnetic rod could provide a stronger magnetic flux, and therefore, a larger induced voltage in the secondary coil, the mechanical properties of ferromagnetic materials are inferior compared to those of steel.

The output of the VCT is an amplitude modulated AC voltage. In order to obtain a DC voltage which is directly proportional to the position of the core, the output of the VCT must be demodulated.

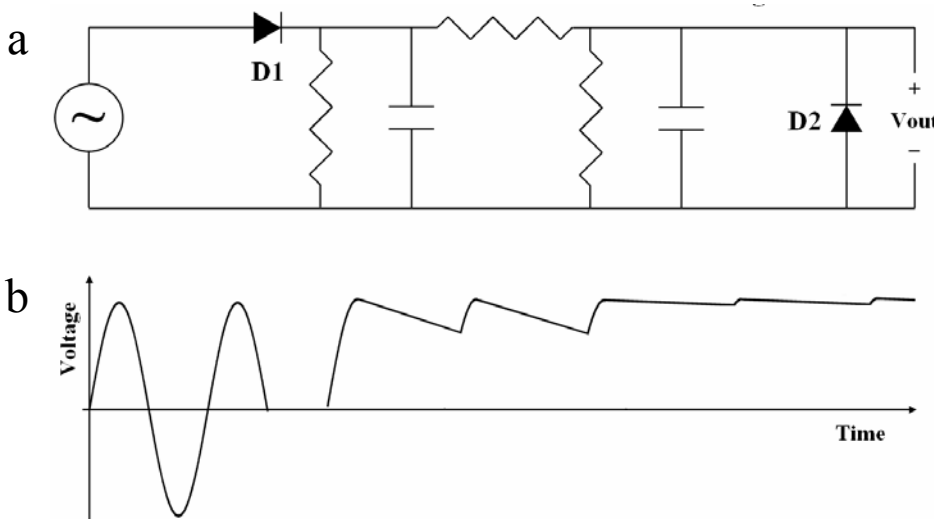


***Figure 16:*** *Half Wave Rectifier Bridge with Filter Network (a) and associated output waveform (b)*

Figure 16a shows a half wave bridge rectifier with a filter network which is used for the rectification of the induced AC voltage in the VCT. The voltage source is the induced voltage in the secondary coil of the VCT and the output voltage (Figure 16b) is the rectified DC signal which is sampled by a 12 bit data acquisition board. Diode D2 is not needed in the rectification of the AC input signal, but is present to prevent the data acquisition computer from electronically loading the VCT in the event of a hardware failure. The AC voltage measured from the VCT and its transformation to a DC signal are shown in Figure 16b. The addition of capacitance reduces the perturbations in the output voltage of the circuit.

In the present configuration, the VCT is constructed by wrapping 34 gauge magnet wire around a nominal 8 mm diameter glass tube, which serves as the cylinder cavity

(Figure 15). The secondary coil is made with the same wire and is wrapped directly on top of the primary coil. The secondary coil, however, has twice as many turns as the primary, giving a turns ratio of 2 and thus amplifying the output voltage as shown in Equation 13. Due to the compact nature of the fluidic actuator, a greater turns ratio could not be accommodated.

A relatively low (7 KHz) excitation frequency was originally selected in order to minimize high frequency noise in the system. However, higher excitation frequencies yield greater output voltages as shown in Figure 17, where the demodulated output voltage range is the voltage difference in the output of the VCT (before amplification) given by moving the piston through its entire range of motion. Demodulated output voltage range also increases as the excitation amplitude is increased.

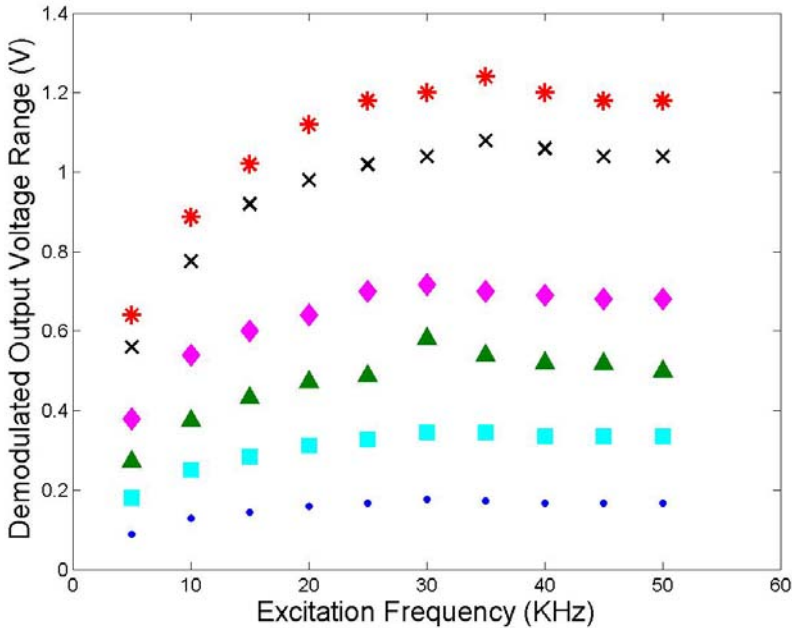


***Figure 17:*** *Demodulated output voltage range as a function of excitation frequency for excitation amplitudes of 2.5(•), 5(■), 7.5(▲), 10(♦), 15(×), and 17.25(*) Vpp*

Using an excitation voltage of 7 KHz (17.25 Vpp) and amplifying the output signal of the circuit shown in Figure 16 using an instrumentation amplifier yields a DC output voltage of 0-5 V as shown by the calibration curves in Figure 9.

## 3.3 VCT Characterization

Because a small change in the position of the core results in a change in the induced voltage. The resolution of the VCT depends on the ability to resolve this voltage. The limiting factors are the resolution of the data acquisition board, and the electric's noise. The sensitivity of the VCT is determined from its calibration curves (Chapter 2).

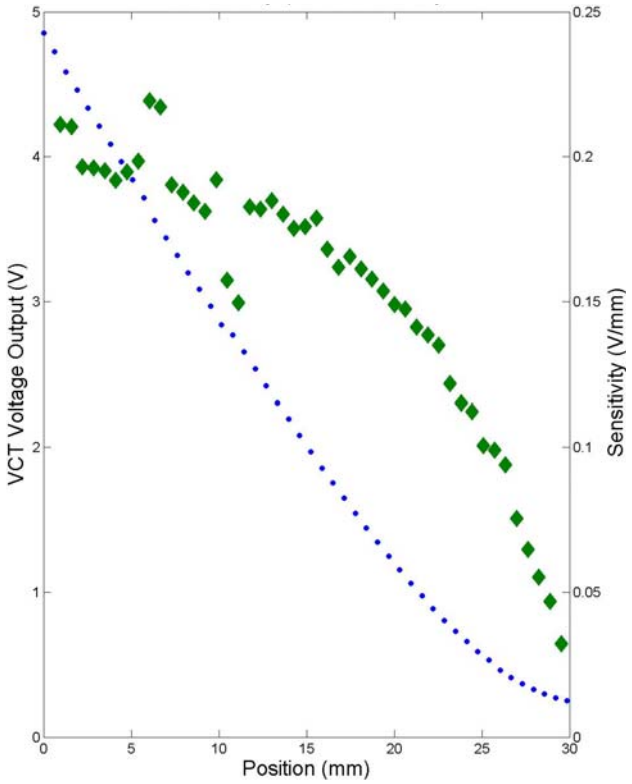


***Figure 18:*** *VCT Sensitivity (♦) and VCT Voltage Output (•)*

Figure 18 shows the output voltage and corresponding sensitivity of the VCT obtained using the calibration technique described in section 2.4.2. These data show that the

sensitivity of the VCT decreases as the piston moves up. At the top of the range of motion (30 mm) the length of the primary coil which is engaging the magnetic core of the VCT is smaller. Given that the resolution of the data acquisition board is 0.24 mV the theoretical resolution of the VCT is nominally 0.008 mm. However, the actual resolution of the VCT is limited by the noise on the output signal, which can be quantified by the standard deviation of the measured piston position at different locations throughout its range of motion. The variation of the standard deviations, or resolution, of the piston position (based on 10,000 samples of the variable core transformer and the optical displacement measurement system) as a function of piston position is shown in Figure 19.

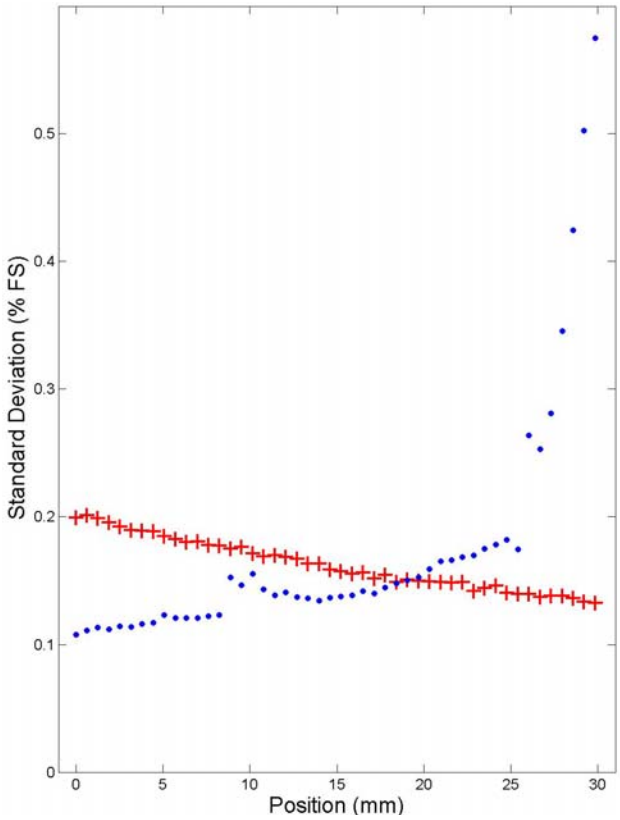


***Figure 19:*** *Standard Deviation of Piston Position as Measured by the variable core transformer (•) and optical displacement measurement system (+)*

The standard deviation of the VCT signal increases dramatically from approximately 25-30 mm due to end effects. This happens when the piston is fully extended (30 mm) and not while the piston is fully retracted (0 mm) because the Teflon seal in the bottom of the piston extends into the primary and secondary coils approximately 17 mm, which stops the actuator shaft before it reaches the end of the coils of the VCT. While the Teflon top seal extends into the glass cylinder, it only extends into the primary and secondary coils approximately 3 mm. Therefore, when the actuator shaft is in its fully extended position it is only partially immersed in the changing magnetic flux of the primary coil, which produces an induced voltage which has more noise than when the shaft is more fully engaged by the primary coil. Averaging the standard deviation values (Figure 19) yields an average resolution of the VCT of 0.17% full scale and an average resolution of the optical displacement measurement system of 0.16% full scale, with respective standard deviations of 0.1% full scale and 0.02% full scale. The repeatability error as a percentage of the Full Scale (FS) of the piston's range of motion is given by (Figliola 2000)

$$e_R = \frac{2 * S_x}{FS} * 100 \tag{14}$$

where $S_x$ is the standard deviation of measured position of the piston. Figure 20 shows the repeatability error of the VCT has an identical trend as the standard deviation of the VCT. This is because the repeatability error is determined by scaling the standard deviation of the measured position of the piston as shown in Equation 14.

The overall errors of the optical displacement measurement system and the VCT are calculated by the addition of the repeatability error and the bias error (section 2.4.2) as

well as the addition of the error due to drift and hysteresis. However, the calculated drift and hysteresis errors of both the optical displacement measurement system and the VCT are less their respective resolutions. Therefore, the overall errors are calculated by combining Equation 7 and Equation 14 as shown in Equation 15 (Figliola 2000).

$$e_{overall} = P_T - P_S + 2S_x \tag{15}$$

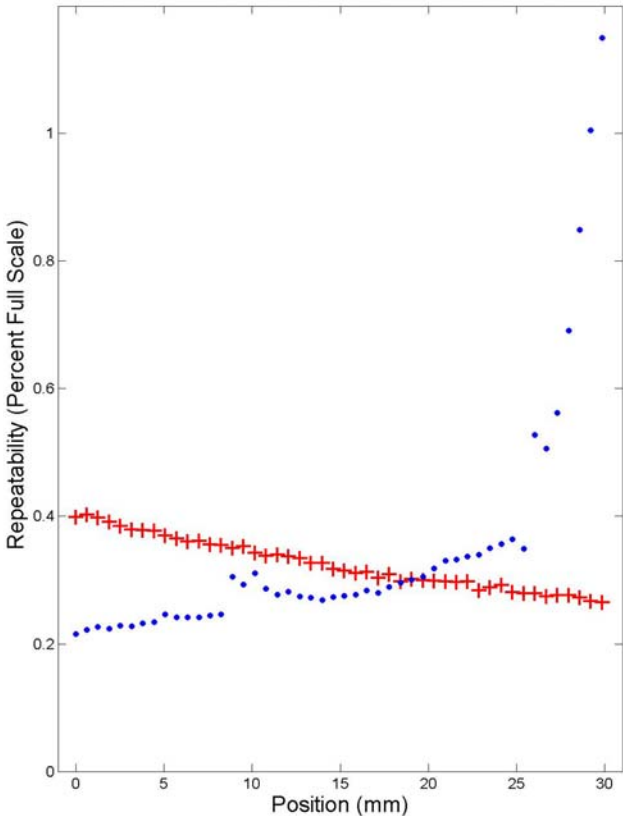


***Figure 20:*** *Repeatability of VCT (•) and optical displacement measurement system (+)*

Figure 21 shows the overall errors of the piston position as measured by the optical displacement measurement system and the VCT as a function of piston position.

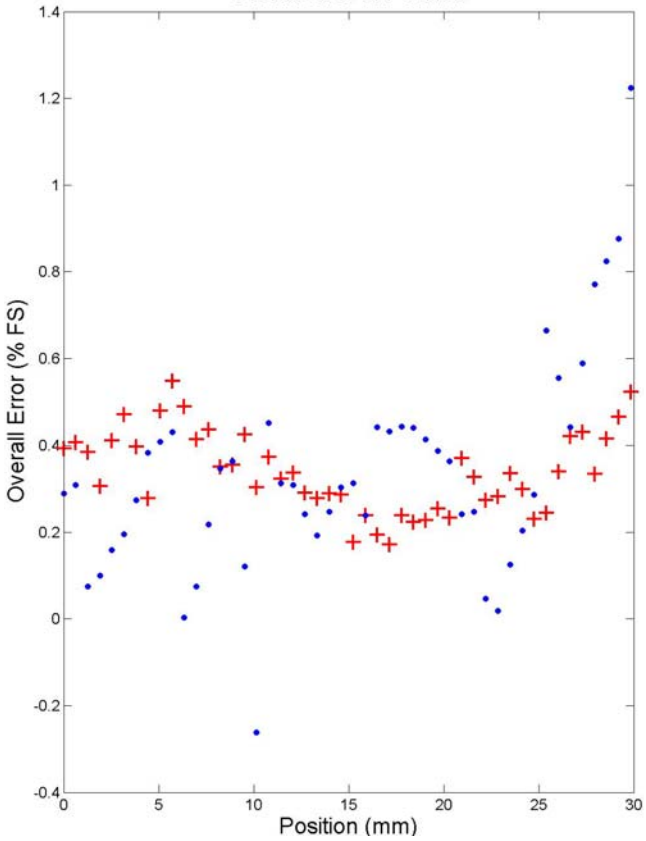


***Figure 21:*** *Overall Errors of the VCT (•) and optical displacement measurement system (+)*

The overall error of the VCT is comparable to the optical displacement measurement system for the majority of the range. Even at the edges, the VCT is still accurate to less than 0.4 mm, which is approximately 1.3 % FS. Comparison of Figure 20 and Figure 11 (chapter 2) shows that when the overall error of the VCT deviates from total error of the optical displacement measurement system (25-30 mm) there is no deviation in the bias error, but there is a variation in the repeatability error. Therefore, the increase of the overall error of the VCT through the approximate range of 25-30 mm is largely attributed to the repeatability error of the VCT.

# CHAPTER 4

# SYSTEM CHARACTERIZATION

This chapter focuses on the characterization of the system and its individual components. An overview of the closed-loop control algorithm is presented in section 4.1. The details of the system implementation of the Proportional Integral (PI) controller used in this work are presented in section 4.2. Section 4.3 describes the tests which are conducted to characterize the response of the PI controller and the solenoid valves. The data management techniques used for the presentation of data in this work are described in section 4.4. The velocity and acceleration of the piston are computed from time traces of its trajectory and are presented in section 4.5. Pressure measurements are used for diagnostics and are presented in section 4.6. The pressure measurements are also used to calculate the friction forces acting on the piston, which are presented in section 4.7.

## 4.1 Closed – Loop Controller

A closed-loop PI controller is used to control the position of the piston based on trajectory measurements obtained from the Variable Core Transformer (VCT). In a closed-loop control system, (Figure 22) feedback allows for the system output to be continuously compared to the desired system output.

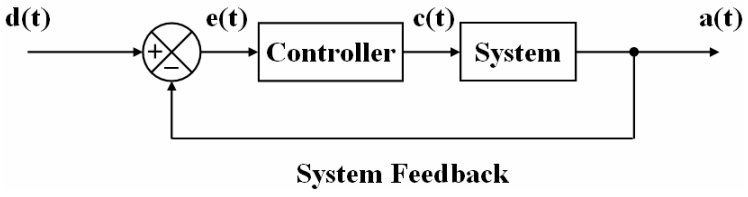


***Figure 22:*** *General Form of Closed-Loop Control System*

The output of the controller and the desired output of the system are defined as c(t) and d(t) respectively. As seen in Figure 22, the controller output, c(t), is used as an input parameter to the system, and a(t) is the corresponding system output. The difference in the desired output of the system and the output of the system is represented by e(t) and is defined as the system error, as shown mathematically in Equation 16 and schematically in Figure 22.

$$e(t) = d(t) - a(t) \tag{16}$$

However, a controller using only the system error to control a given parameter of interests often does not provide sufficient control because a very small system error can cause a controller output which can lead to system instability. Therefore, more sophisticated control algorithms are usually employed. One such control algorithm is a specific form of closed-loop control known as Proportional Integral, or PI control. PI controllers provide greater control than a controller which uses only the system error by introducing a user specified proportional gain as well as the calculation of an integral error and a subsequent integral gain. Figure 23 shows the implementation of a PI control algorithm.

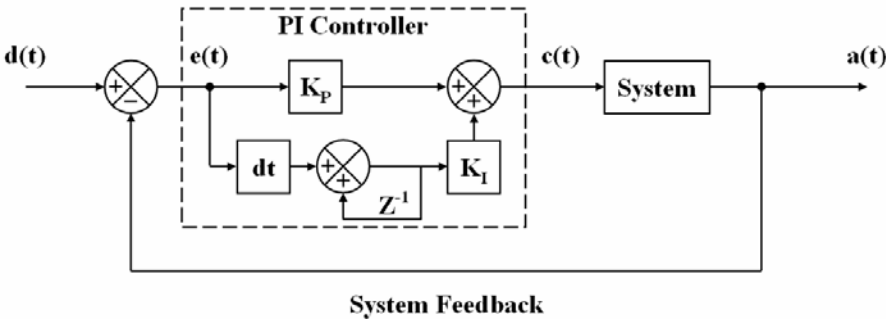


***Figure 23:*** *PI Closed-loop Control Algorithm*

The proportional contribution of the controller algorithm is the product of the system error, e(t), and a user specified proportional gain, $K_P$, which affects the controller output, c(t), as defined by Equation 17.

$$c(t) = K_P * e(t) \tag{17}$$

With a proportional control algorithm, the controller output changes in proportion to the system error by a factor of $K_P$. The integral contribution of a PI controller is the integration of the system error with respect to time multiplied by a user specified integral gain, $K_I$ as shown in Equation 18.

$$c(t) = K_I * \int e(t) * dt \tag{18}$$

With an integral controller, any system error eventually grows to a detectable state, which increases the accuracy by which the controller can control the output of the system. The mathematic combination of Equation 17 and Equation 18 gives the output of a PI controller as shown in Equation 19 while their schematic combination is shown in Figure 23.

$$c(t) = K_P * e(t) + K_I * \int e(t) * dt \tag{19}$$

A PI controller supplies an output which is proportional to the system error and also integrates that system error over time for increased accuracy. The value of this controller output is used to modify the physical system and is based on the user specified values of $K_P$ and $K_I$ as well as the continuously calculated system error. The controller output is used as an input parameter to the system being controlled.

## 4.2 System Implementation of Closed – Loop Controller

The PI controller controls the position of the piston using trajectory measurements of a Variable Core Transformer (VCT) by actuating two solenoid valves which are embedded in the fluidic actuator described in section 2.1. However, certain modifications to the general description of a PI controller presented in section 4.1 are necessary.

In order to optimize the control loop rate, two computers are utilized in this work. The control-loop is implemented on a laboratory PC using LabView RT while a separate data acquisition PC using LabView is used to sample and save the position of the piston and the pressure of the working fluid in various system locations. With this setup, the data acquisition computer handles the load of saving data while the target machine's only task is to run the control loop, thereby isolating the control loop and alleviating potential internal system interruptions associated with saving data. The PI controller algorithm (Figure 23) is written in LabView RT and downloaded onto the target.

As show by Equation 16, the control-loop requires a desired system output as a continuous input parameter. While the controller will accept any analog function as an input parameter, a square wave, generated by a function generator (HP 33120A), is chosen in order to move the piston between two predetermined positions. Using the function generator to generate the desired values allows for precise flexible control of the controller input parameters, and therefore the desired output of the piston position.

Figure 24 shows the overall system implementation of the PI controller shown in Figure 23 and its interaction with the physical setup. Digital output values are produced by the PI controller software, which runs on the target machine, based on the output value of the PI controller and used as input values to the valves in the physical system. The actuation of V1 or V2 moves the piston down or up respectively as described in section 2.1. After the appropriate valve has been actuated the position of the piston is measured by the Variable Core Transformer (VCT) and used to calculate an updated system error value, which is used as an updated input parameter to the PI controller.

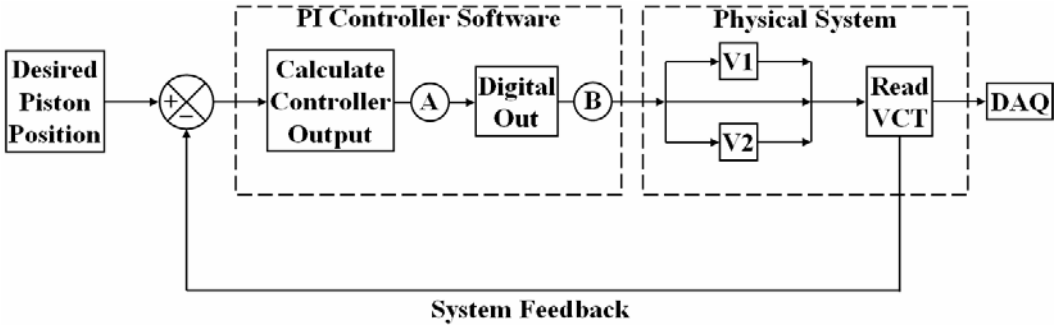


***Figure 24:*** *PI Controller Implementation showing PI controller software and physical system components*

A proportional integral controller is used because a proportional control algorithm is only partially functional for the control of the non-proportional solenoid valves used in this work. This is because the only valve configurations are fully open and fully closed. Therefore, as the system error decreases, the controller output decreases to the point that only a slight change in the system output is needed to match the desired output, which is not attainable by fully opening, or closing, the valve. As a result, the valve is fully opened and closed rapidly to try to achieve the desired system output, which creates unwanted oscillations. A possible solution is to specify an error bound on the system output, within which the controller does not output anything, allowing the system to

maintain its current state. This error bound is necessarily introduced at location A in Figure 24, after the controller operations and before the digital output operation. While the addition of an error bound alleviates problems of system instabilities, it decreases the accuracy with which the controller can control the system output by introducing the possibility of a steady state bias error. One of the solutions to this issue is to incorporate integral control in addition to proportional control, yielding a PI controller output as governed by Equation 19. As seen in Figure 24, there are three distinct possible output values from the PI controller software, which are detailed in Table 2. The controller output voltages are sent to solid state relays which actuate the valves in order to move the piston as indicated by the last column of Table 2

***Table 2:*** *Controller Output Configuration*

| **Controller Output Configuration** | **Controller Output Voltage** | | **Physical System Meaning** |
|---|---|---|---|
| | **Channel 1 (V1)** | **Channel 2 (V2)** | |
| 1 | 5 | 0 | Move Piston Down |
| 2 | 0 | 0 | No Piston Motion |
| 3 | 0 | 5 | Move Piston Up |

When the position of the piston, as measured by the VCT, is above the user specified desired piston position, the output of the controller is described by configuration 1 shown in Table 2. Similarly, when the measured position of the piston is below the desired piston position configuration 3 is utilized. If the piston position is within the user specified error bound described above then configuration 2 is used and the piston maintains its current position. An error bound of 1 mm is chosen for this work because it is greater than the system error (section 3.3) and is attainable with noise in the system.

As described by Equation 18, any system error will cause the integral error to grow. Therefore, if the desired piston position is in the form of a square wave, which causes an instantaneous system error, then while the appropriate solenoid valve is fully opened to reduce the system error the integral error will also begin to grow. The fact that the integral error begins to grow the moment a system error is detected is not an issue. However, complications arise in the fact that the valve is already fully opened and any additional growth of the integral error will not achieve the desired result of further opening the valve. Therefore, if the integral error is allowed to grow at the onset of a system error then when the piston reaches the desired position the integral error will still be non-zero. This non-zero integral error will produce a non-zero PI control software output, which will move the piston past the desired piston position and unnecessarily decrease the accuracy of the controlled piston position. For this reason a user specified bound is added to the integral error which only allows the integral error to grow while the system output is close to the system error bound. Therefore, a proportional controller is effectively used to move the piston close to the desired piston position and an integral controller is effectively used to alleviate any steady state bias error in the controlled piston position.

Controlling only position and using on-off solenoid valves makes it impossible to control the velocity or acceleration of the piston because the valve is either fully open or fully closed. Therefore, if an arbitrary curve is used as the desired piston position, then the PI controller software will move the piston either up or down to reduce the error. However, as shown in Figure 25, if the desired position is a curve then the resulting motion of the

piston can not match it because the only options that the controller has are to fully open or fully close the valves, which gives the position response shown in Figure 25. It is noteworthy that the "steps" in position are attributable to the fact that the position is controlled by on-off valve actuation. The response time of the valves is on the order of 1-2 ms, and the steps shown in Figure 25 are on the order of 30 ms.

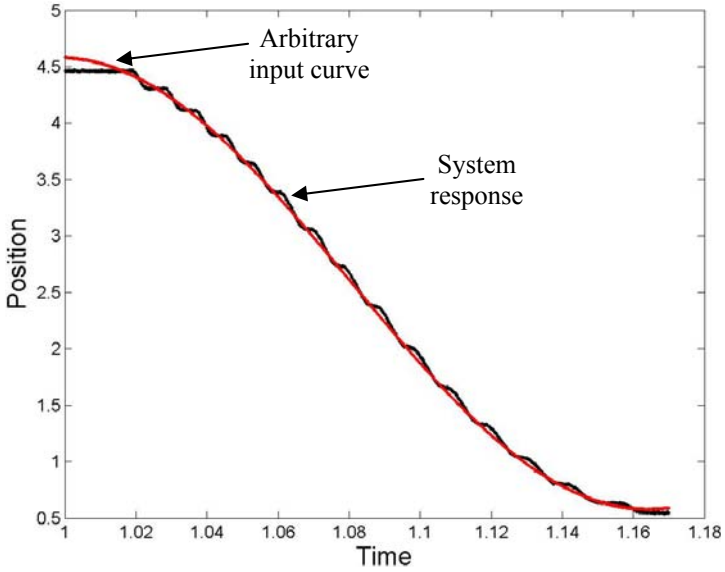


***Figure 25:*** *System response to arbitrary input curve*

## 4.3 Control-Loop Characterization

This section describes the tests that are conducted in order to determine the performance of the PI controller described in section 4.2. Sampling the digital output of the controller at a rate of 140 KHz for 14,000 cycles of the control-loop gives an average control-loop rate of 687 μs with a standard deviation of 8 μs, as shown in Figure 26. The data shown in Figure 26 represents both upward and downward actuation of the piston and is approximately normally distributed about 687 μs; confirming that the control-loop response time is independent of the direction of the actuation of the piston.

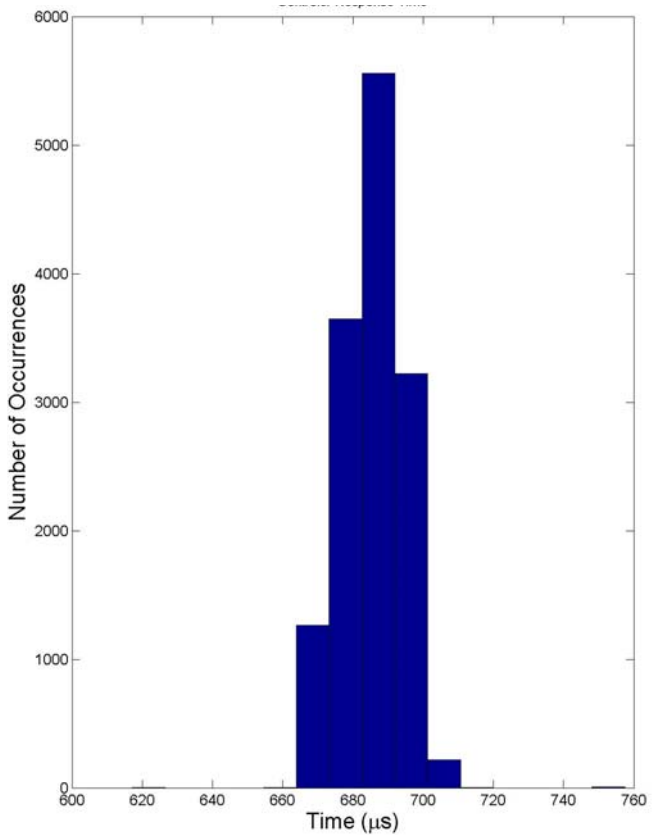


***Figure 26:*** *Histogram of Controller Response Time*

As described in section 4.2, the controller has analog input values (function generator) for the desired system output and the piston position (VCT) as well as two digital outputs which correspond to the actuation voltages for the valves as described by Table 2. The channels on the data acquisition board need to be initialized before any signals can be passed through the board. This initialization takes place when the control-loop program is started, but before the controller actually starts as illustrated by Figure 27.

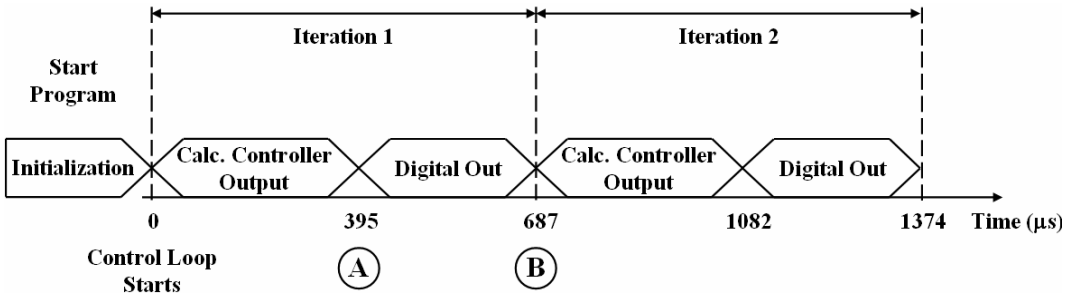


***Figure 27:*** *Controller Timing Diagram*

The portions of the controller timing diagram labeled as A and B in Figure 27 correspond to the same labeled positions in PI controller implementation diagram shown in Figure 24. Therefore, the controller takes an average of 395 μs to sample the appropriate analog channels and compute the controller output. The creation and output of the TTL signals needed to actuate the valves consumes an additional 292 μs to bring the control-loop rate to approximately 1455 Hz.

As mentioned in section 4.2, the valves are actuated by TTL signals through solid state relays. Figure 28 shows the response time of one of the valves obtained by recording the voltage across a shunt resistor in series with the output of the solid state relay (sampled at 10 KHz for 500 cycles of the piston). Figure 28 also shows the pressure response. When the voltage is first applied to the solenoid valve the solenoid has to induce high enough voltage into the coil of the valve to switch it mechanically. When the valve switches, the current through the coil changes and produces a local minimum in voltage (for $0.6<t<2.8$). The pressure difference across the valve begins to change when the valve is opened.

V1 has an average rise time of 1.68 ms and a standard deviation of 0.17 ms and V2 has an average response time of 1.28 ms with a standard deviation of 0.40 ms, which are within the manufacturer's specified 1-2 ms response time. The system is driven with 15 psi in the pressure reservoir. For this reason, the pressure difference across the valve at the time of excitation is 15 psi. As seen in Figure 28, the pressure difference across the

valve does not change until approximately 1.7 ms, further confirming the response time of the valve.

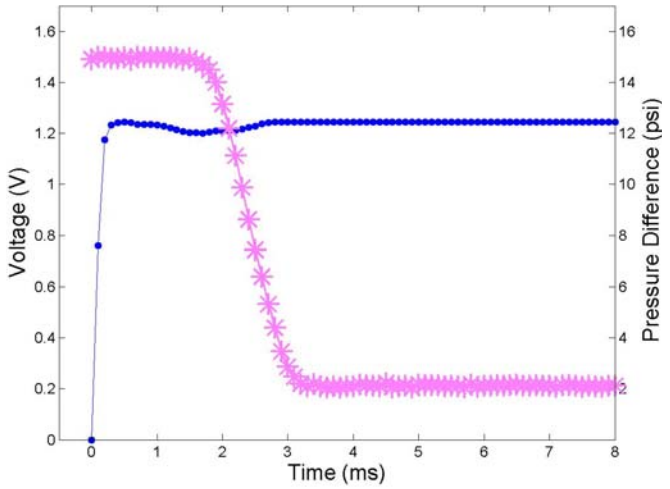


***Figure 28:*** *Average Voltage (•) and Pressure Response (*) for V1 (500 Cycles) with a driving pressure of 15 psi*

## 4.4 Data Management

Due to the cyclic nature of the piston's motion, it is desirable to present phase averaged position and pressure data. The stroke is the maximum displacement of the piston (either bottom to top or top to bottom) within the cylinder while a cycle is defined as an upward stroke followed by a downward stroke. Unless otherwise specified, all of the present data are measured during 20 consecutive cycles of piston motion. All position and pressure data is phase locked to the desired system output and phase averaged. The upward and downward piston motion are separated to provide the ability to analyze each directional data set individually.

With a signal to noise ratio of the position, measured by the variable core transformer, of approximately 161, the averaged cyclic position data is further reduced by passing a

window over it and averaging the data inside the window. The resulting single data point from each window is reassigned to the time which corresponds to the middle time step of each window.

## 4.5 Velocity and Acceleration of Piston

Piston position data is recorded at 1 KHz for 20 100 mHz cycles of the piston and reduced using the method described in section 4.3. The piston position data y($i$) is numerically differentiated using central differencing to obtain velocity and acceleration approximations of the piston such that

$$v_P(i) \approx \frac{y_{i+1} - y_{i-1}}{2\Delta t} - O(\Delta t^2) \tag{20}$$

and

$$a_P(i) \approx \frac{y_{i-1} - 2y_i + y_{i+1}}{\Delta t^2} - O(\Delta t^2) \tag{21}$$

(Press 1992) where Δt represents the time difference between two adjacent data points and y(i) represents the position of the piston. The errors of the velocity and acceleration approximations are on the order of $\Delta t^2$. With a time difference (Δt) of 1 ms, the errors in the velocity and acceleration are both significantly less than 0.01% of the calculated values.

Figure 29a and b show the piston trajectories for 20 cycles of upward and downward piston motion respectively as a function of time for multiple driving pressures. Since each line type in Figure 29 represents 20 cycles, the minimal dispersion as shows the

stability of the velocity of the piston. The time required for the piston to move through its range of motion increases as the pressure is decreased (5 seconds for 6 psi vs 0.8 seconds for 25 psi). Note that at 6 psi (the system's lowest operating pressure) the piston's motion does not reach the end point within the shown time.

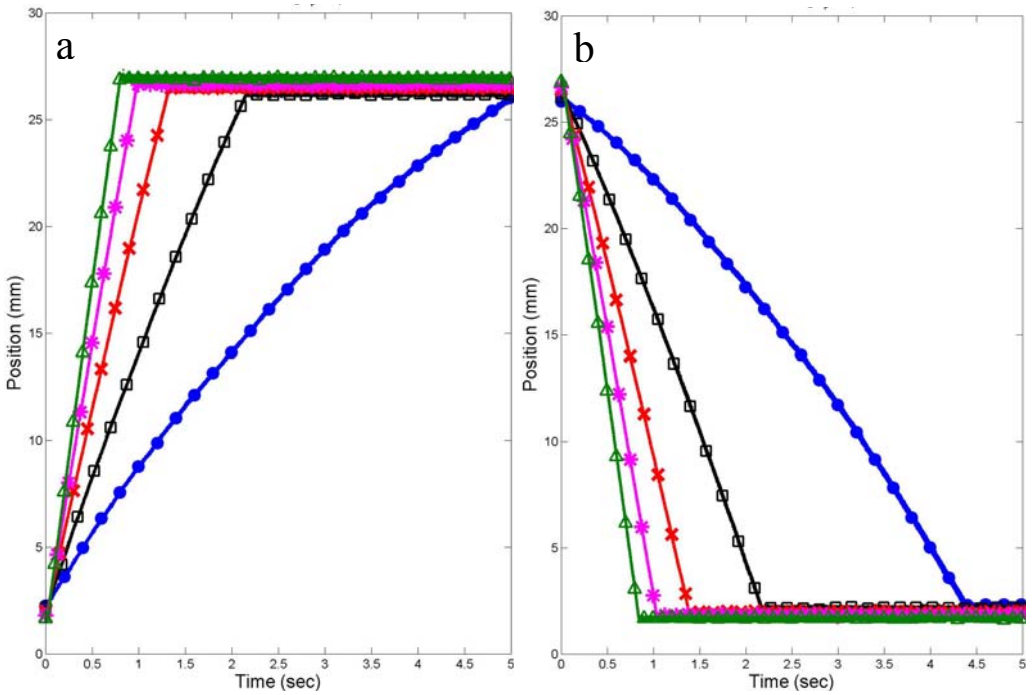


***Figure 29:*** *Piston position for upward (a) and downward (b) motion of the piston respectively for driving pressures of 6 (•) 10 (□) 15 (×) 20 (*) and 25 (Δ) psi*

Figure 30 shows samples of the velocity and acceleration approximations of the upward and downward motion of the piston as a function of position for multiple driving pressures.

Figure 30a and c represent the upward motion (2-28 mm) of the piston while Figure 30b and d represent the downward motion (28-2 mm) of the piston. Therefore, the velocity of the piston is globally increasing as it moves down and globally decreasing as it moves up.

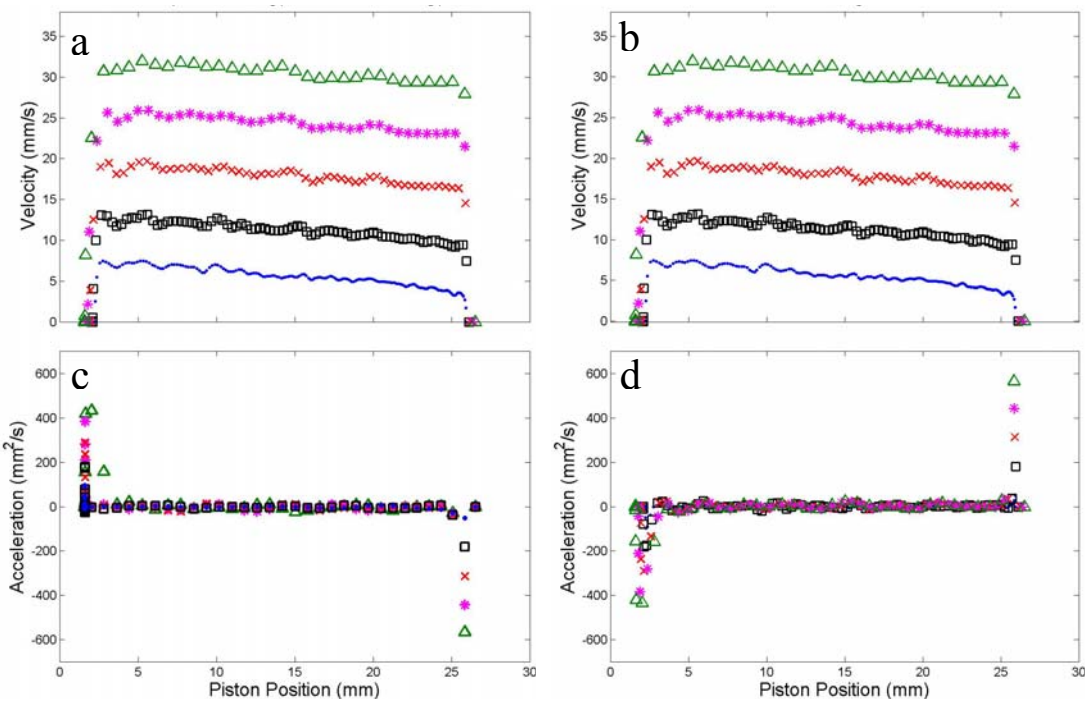


***Figure 30:*** *Piston velocity and acceleration for upward (a,c) and downward (b,d) motion of the piston respectively for driving pressures of 6 (•) 10 (□) 15 (×) 20 (*) and 25 (Δ) psi*

A comparison of Figure 30a and b shows that the downward velocity of the piston is generally greater than the upward velocity of the piston. This is because the viscous losses associated with the channels employed for the downward motion of the piston are less than those associated with the upward motion of the piston due to the internal geometry of the fluidic actuator. Comparison of Figure 30c and d shows that the acceleration of the piston as it moves up and down are approximately zero while the piston is in motion when compared to the respective accelerations at the commencement and termination of the piston's motion. The piston accelerations are higher for both the upward and downward motion of the piston when the piston is beginning its motion than they are when the piston is ending its motion. This is because there is a larger pressure spike when the valves are opened than there is when the valves are closed.

The velocities shown in Figure 30a and b are averaged over the time that the piston is in motion and plotted in Figure 31. As seen in Figure 31, the velocity of the piston varies linearly with the variation of the driving pressure for both the upward and downward motion of the piston.

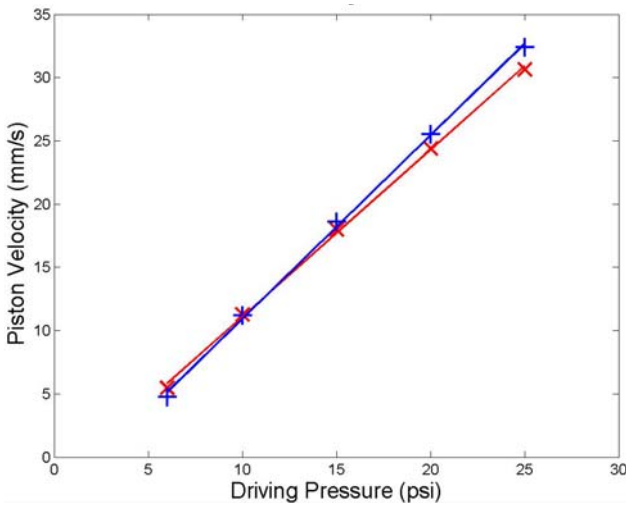


***Figure 31:*** *Average piston velocities as a function of driving pressures upward (×) and downward (+) motion of the piston*

As noted above, the piston accelerates as is moves down and decelerates as is moves up. The reason is a misalignment of the piston with the piston rod, which is described in more detail in section 4.7. The range of piston motion shown in Figure 30 does not represent the entire range of motion of the piston. The piston is commanded to move through the middle 25 mm of its 30 mm range of motion to prevent a potential collision of the piston with the top or bottom of the cylinder cavity.

## 4.6 Pressure Measurements

Figure 32 shows the fluid channels that are utilized for piston actuation. When the piston is commanded to move, fluid moves from the pressure reservoir to the fluidic actuator,

through valve V1 or valve V2, through the cylinder cavity and into the return tank. As described in section 2.2.2, the fluidic actuator is instrumented with six pressure ports. Two transducers, T1 and T2, are used to monitor the pressure in ports 1-6 (Figure 32) while T3 is connected to port 7.

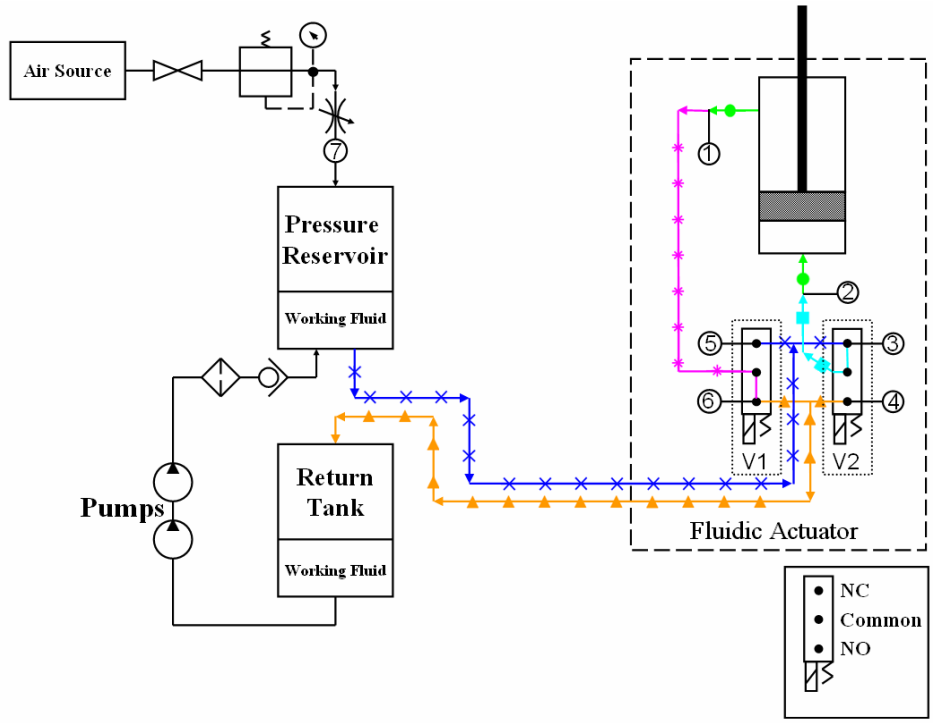


***Figure 32:*** *Fluidic system schematic showing fluid paths from pressure reservoir to fluidic actuator (), across V1 (), across V2(),across the piston (), and into the return tank ()*

The pressure difference across the piston is of particular interest because it corresponds to the force that the piston produces at a given operating pressure. Figure 33 shows the pressure differences across the system components shown in Figure 32 at a driving pressure of 15 psi. The pressure differences across valves V1 and V2 for the upward and downward motion of the piston at 0 mm and 22 mm are 15 psi because the system was driven with 15 psi for these measurements. Therefore, the pressure difference across the

valve when the valve is closed is equal to the driving pressure of 15 psi. Comparison of Figure 33a and Figure 33b shows that the pressure difference across the piston generally decreases in magnitude as a function of position for the downward moving piston and generally increases in magnitude as a function of position for the upward moving piston.

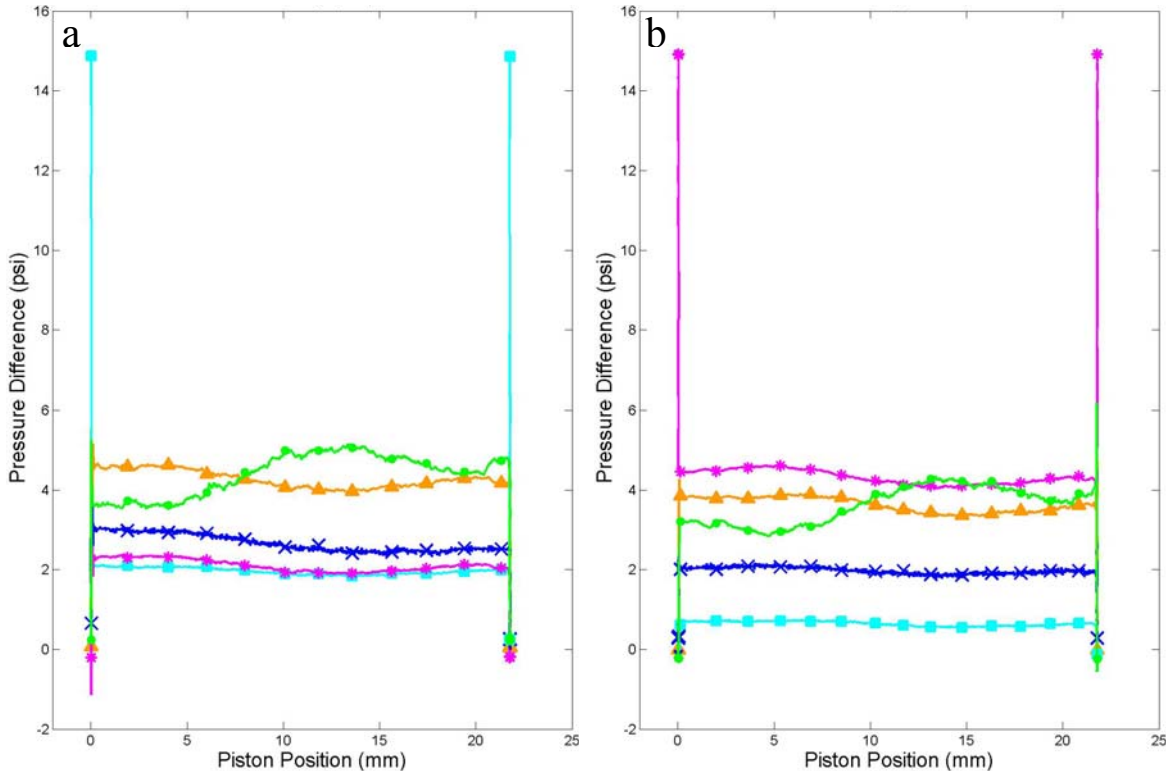


***Figure 33:*** *System pressure difference for upward (a) and downward (b) motions of the piston (symbols as in TFigure 32)*

However, all of the other system pressure differences shown in Figure 33 exhibit the opposite trend; decreasing in magnitude as a function of position for the upward moving piston and increasing in magnitude as a function of position for the upward moving piston. Comparison of Figure 33a and Figure 33b shows that the pressure variations for the upward and downward motion of the piston are nearly identical. The large range of motion over which the major variation in the pressure difference across the piston occurs (5-20 mm) indicates that the fluctuations in pressure are not location specific and are,

therefore, not attributable to localized surface irregularities on the shaft, cylinder, or top seal.

The reason that these pressure difference profiles generally increase as a function of piston position is because the piston head is actually mounted off center. This misalignment is present because when the piston rod was glued to the piston, the piston rod was centered on the piston head by inserting the piston rod to a location approximately 5 mm from the bottom of the cylinder and leaving it there until the glue dried. Since the glue was allowed to dry at this location there is no side loading on the piston due to misalignment when the piston position is approximately 5 mm. For this reason, the pressure differences across the piston for the upward and downward motion of the piston have minimums at approximately 5 mm (Figure 33). Figure 34 shows a schematic of the piston inserted into the cylinder at depth d. The side loading on the piston increases as the piston moves up because distance d is the length of the shaft that is flexed as the piston moves. As the piston moves up, distance d decreases, which increase the rigidity of the shaft, and therefore, the force needed to flex the shaft.

The increasing side loading on the piston slows the ascent of the piston and therefore increases the pressure difference across the piston head. This also decreases the pressure differences across all of the other fluid channels because the pressure difference across all of the channels is proportional to fluid velocity, and the fluid velocity is decreasing due to the decreasing velocity of the piston.

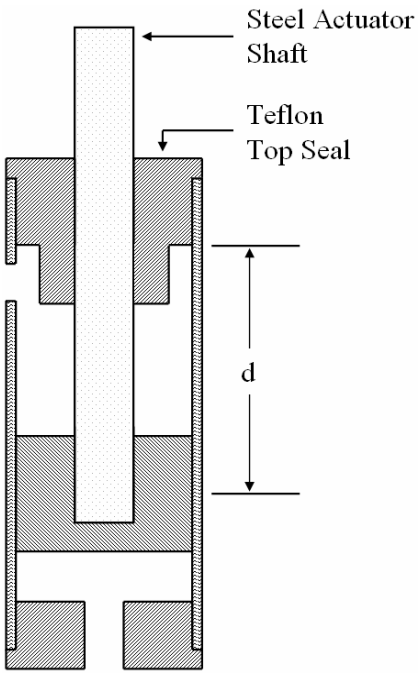


***Figure 34:*** *Schematic of piston showing steel actuator shaft, Teflon top seal, and piston depth d.*

This is visible in Figure 33a by the increase in pressure difference across the piston from approximately 5 to 13 mm and in Figure 33b by the decrease in the pressure difference across the piston over the same range of motion. The downward motion of the piston has the opposite behavior as the upward moving piston because as the piston moves down the side loading is decreased and the piston accelerates downward, decreasing the pressure difference across the piston head and increasing the pressure differences across the other fluid channels.

Because the upper and lower cylinder cavities are connected to the common ports of the valves (Figure 32) and the normally closed ports of both valves are connected to the pressurized fluid, only one valve needs to be activated to actuate the piston (V1 and V2 for motion upward and downward respectively). The pressure differences across V1 and

V2 change simultaneously for the upward and downward motion of the piston. The characteristic response times are somewhat different (e.g. 1.68 ms vs 1.28 ms for up/down motions respectively).

## 4.7 System Friction Forces

This section describes the test stand that was developed to characterize the friction forces acting on the piston. The contributions to friction are the friction force due to the Teflon top seal ($f_{teflon}$), the inertia of the fluid in the upper cylinder cavity ($f_{inertia}$), and the reactionary force acting on the side of the piston head due to the misalignment of the actuator shaft ($f_{side}$). Figure 35a shows the free body diagram of the upward moving piston while Figure 35b shows the labeled system components. The accompanying force balance equations are shown in Equation 22. As seen by Equation 22, the friction force due to the side loading on the piston ($f_{side}$) is obtained by using the forces due to the driving fluid in the upper, $(pA)_u$, and lower, $(pA)_l$, cavities, the force due to the weight and acceleration of the piston and shaft and the friction force exerted by the Teflon top seal ($f_{teflon}$).

$$\begin{aligned} \sum F_y : (pA)_l - (pA)_u - Mg - f_{teflon} - f_{side} &= F_{available} \\ (pA)_l - f_{inertia} - Mg - f_{teflon} - f_{side} &= Ma_{piston} \\ (pA)_l - f_{inertia} - M(g + a_{piston}) - f_{teflon} &= f_{side} \end{aligned} \tag{22}$$

As shown in Equation 22, the force due to the driving fluid in the upper cavity has been labeled as $f_{inertia}$. This is done because when the piston is moving up, the lower cavity is pressurized and the upper cavity is connected to the return tank through the pathways

shown in Figure 32. Therefore, the pressure measured in the upper cavity for the case where the piston is moving up is due to the inertia of the fluid along with the friction due to the respective channels. However, the friction force due to the Teflon top seal is unknown. For this reason, an isolated experiment is described whereby the friction force due to the Teflon top seal is obtained.

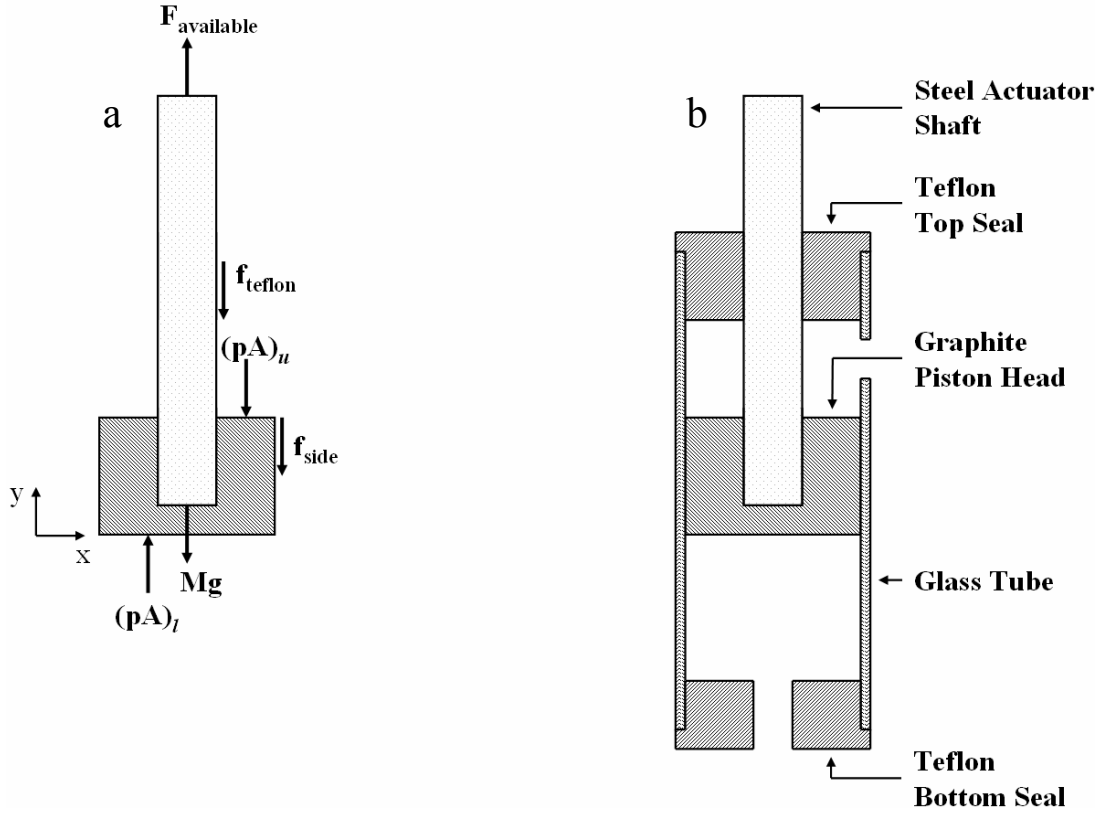


***Figure 35**: Free body diagram for upward motion of the piston (a) and labeled system components (b)*

The friction force test stand (Figure 36) was used to isolate the friction force due to the Teflon top seal from the other friction forces in the system (section 2.3.2). Figure 36 shows the basic structure of the friction force test stand, the forces acting on the piston rod, and the force balance equation during the upward and downward motions of the piston. In this stand, the actuator shaft is pulled through the Teflon top seal by a given weight (40 g). The piston position is measured at 100 KHz by the Optical Displacement

Measurement System (section 2.3.2) for 20 strokes of the piston. The friction force between the Teflon top seal and the steel actuator shaft is obtained by calculating the acceleration of the piston. As shown in Figure 36 (see also section 2.3.2), the friction force test stand does not include the side loading on the piston head within the glass tube.

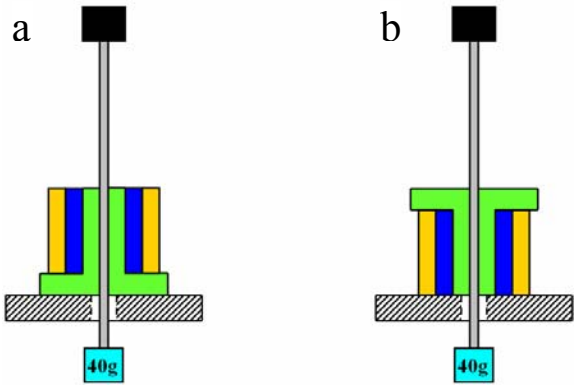


***Figure 36:*** *Friction Force Test Stand for Simulated Upward and Downward Motion of the Piston (Solenoid Not Shown)*

The orientation of the Teflon top seal is changed for upward and downward motions (Figure 36). The calculated acceleration of the piston is used in Equation 23 to obtain the friction acting on the shaft due to the Teflon top seal.

$$\sum F_y : f_{teflon} - Mg = Ma_{piston}$$
$$f_{teflon} = M(g + a_{piston}) \tag{23}$$

Figure 37 shows the calculated velocity and acceleration for upward and downward piston motion respectively.

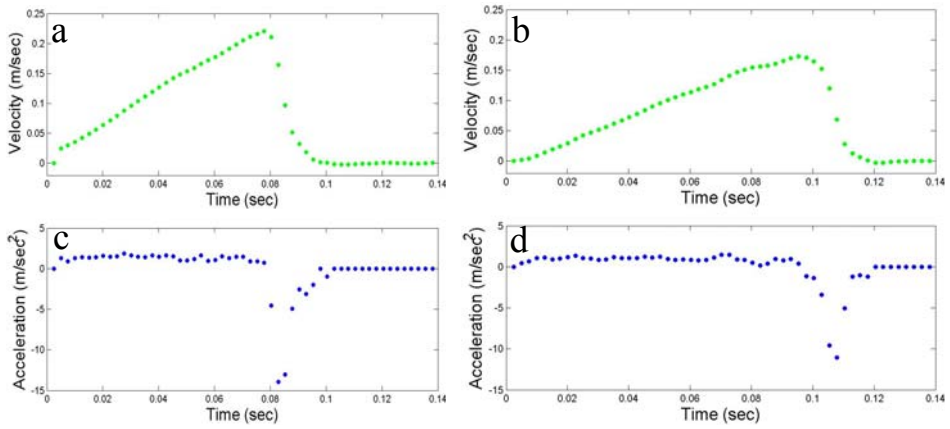


***Figure 37:*** *Velocity and Acceleration for upward (a,c) and downward (b,d) piston motions respectively as obtained from the friction force test stand*

Inspection of Figure 37 shows that the velocity and accelerations calculated from the friction force test stand are time invariant during the motion of the piston, which means that the corresponding friction forces that are calculated from the accelerations can be used as constants in Equation 22. Comparison of Figure 37a and c with Figure 37b and d shows that the piston accelerates faster as it moves up than it does as it moves down because the same distance is traveled in less time. The average acceleration for the upward and downward moving piston are 1.42 m/s$^2$ and 1.05 m/s$^2$ respectively, which yields average friction approximations ($f_{teflon}$) of 0.504 N and 0.522 N respectively. The difference in the friction force is present because the Teflon top seal actually has small helical ridges on the inside of the center hole from the machining process. These small ridges produce a greater friction force when the actuator shaft is moving down than when the piston is moving up, which partially accounts for the decreased acceleration of the downward moving piston as compared to the upward moving piston.

With the isolated measurement of the friction force due to the Teflon top seal ($f_{teflon}$), it is now possible to solve Equation 22 for the friction force which is attributable to the side loading on the piston head ($f_{side}$). Figure 38a and b show the resultant friction force acting on the piston and actuator shaft as well as the friction force due to the side loading on the piston head ($f_{side}$), the friction force due to the Teflon top seal ($f_{teflon}$), and the friction due to the inertia of the fluid ($f_{inertia}$) for the upward and downward motions of the piston respectively. The friction force due to the side loading on the piston head ($f_{side}$) was obtained by solving Equation 22.

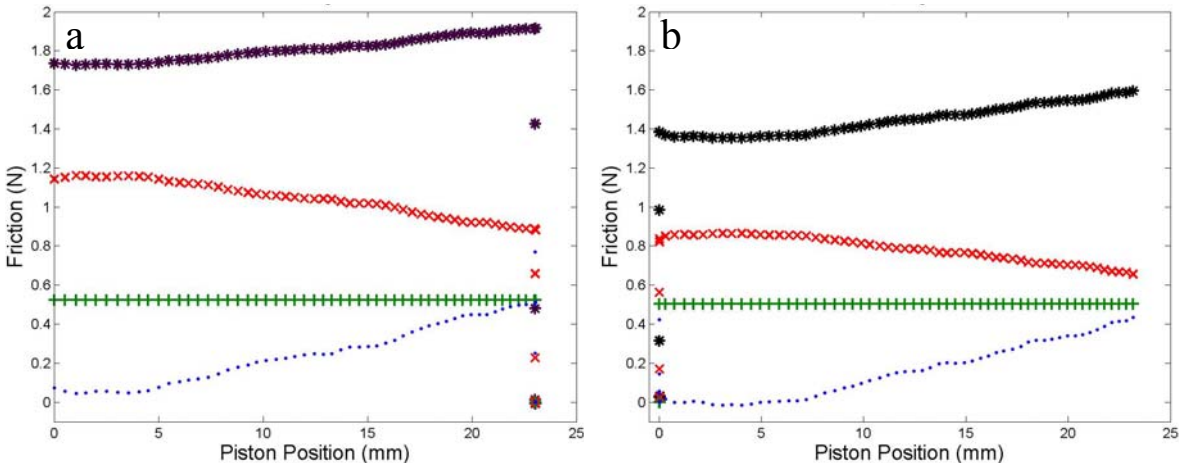


***Figure 38:*** *Friction forces acting on the piston head and actuator shaft $F_{side}$ (•), $F_{teflon}$ (+), $F_{inertia}$ (×), and $F_{total}$ (*) for upward (a) and downward (b) piston motions*

A comparison of Figure 38a and b further confirms that the decrease in velocity for the upward motion and the increase in velocity for the downward motion are a result of the increasing and decreasing side loading on the piston head. Figure 38 shows that as the piston rises, the side load on the piston head continually increases. As the side load increases due to the increased rigidity of the actuator shaft (Figure 34), the piston slows down. This reduction in velocity lowers the viscous losses associated with expelling the

fluid from the upper cavity to the return tank as the piston moves through its range of motion, as seen in Figure 38. The resultant friction force acting on the piston as it moves downward is decreasing for the same reason that the resultant friction force acting on the piston as it moves upward is increasing. As seen in Figure 38, the side loading on the piston head ($f_{side}$) reaches a minimum at approximately 5 mm. This corresponds to the minimum pressure difference across the piston (Figure 33) and confirms that the misalignment of the shaft has an adverse effect on the resultant friction force acting on the piston head and actuator shaft. The pressure (viscous) losses as computed from poiseuille flow are approximately 40% smaller than the measured losses presented in Figure 38. This discrepancy may be attributed to small variations in the internal channel diameter where the tolerance owing to the stereolithography can be on the order of 0.25 mm.

# CHAPTER 5

# CONCLUSIONS

Digital Clay is a tactile array of linear fluidic actuators which provide distributed sensing and position control through the use of an embedded position sensor. Chapters 2-4 discuss in detail the development and characterization of the fluidic actuator. Before the presentation of the conclusions, the implementation of these actuators in a stand-alone tactile-array is described in some detail in section 5.1. Some of the characteristics of Digital Clay are discussed in section 5.2 and potential improvements are discussed in section 5.3. Finally, a summary of the present work is included in section 5.4.

## 5.1 5x5 System Implementation

Figure 39 shows an assembled 5x5 actuator array that integrates all of the components needed to drive a single actuator. The internal geometry of each actuator is identical to that of the actuator characterized in Chapter 2 of this work. However, a number of external modifications were made in order to accommodate an electronics board and allow the module to be easily plugged into the base plate and seal properly. When the fluidic actuator is plugged into the fluidic base plate it also plugs into an electronics board which contains communication ports for the control of each individual actuator. A pressure tank (pressurized by air) supplies pressurized fluid to the actuators through the fluidic base plate shown in Figure 39. The low pressure fluid from each actuator flows into the return tank and is pumped into the pressurized tank by built-in pumps.

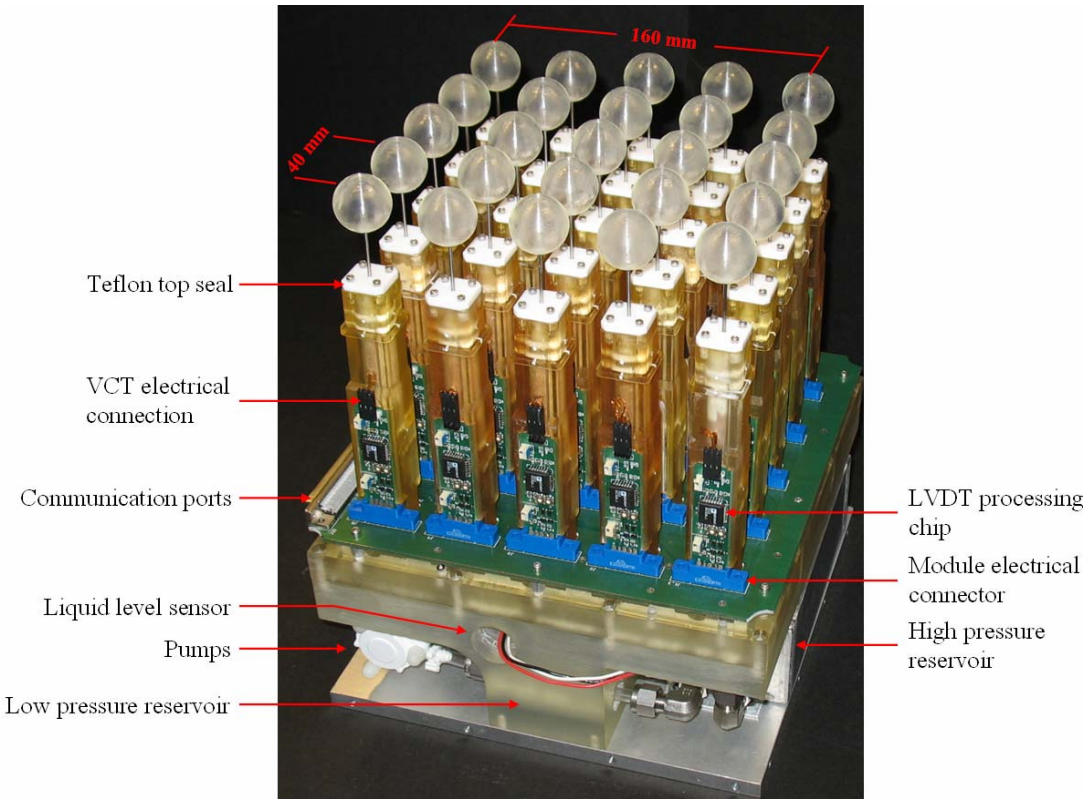


***Figure 39:*** *5x5 Implementation*

The pistons of the array are equally spaced on a square grid (3x3 cm) placed on a larger base plate. As shown in Chapter 4 (Figure 33), the pressure difference across the fluid line which connects the fluidic actuator to the return tank has nearly the same magnitude as the pressure difference across the piston head. For this reason, the fluid lines used to connect the actuators to the return tank in the 5x5 array are channels which go directly to the fluidic base. This augmentation greatly reduces the pressure difference needed to move the working fluid from the actuators to the return tank by reducing the losses in the channels. This reduction in losses provides a greater pressure difference across the pistons which will yield larger piston speed and force.

In the integrated 5x5 array, a linear variable differential transformer signal processing chip (AD 698AP) is used to excite the primary coil, read the induced voltage in the secondary coil, and demodulate the signal. The use of this chip reduces the hardware volume that is necessary to run the system and increases the modularity of each actuator. The demodulated signal from each actuator is sampled by a data acquisition computer, which is attached to the electronics board through the analog output communications ports. The control algorithm (discussed in section 4.2) is used to control the 5x5 array. However, a packet containing the desired piston positions can be sent over the internet, allowing Digital Clay to be controller remotely.

As discussed in section 4.7, the piston head can become misaligned during the manufacturing process. The method used to attach the piston heads to the piston rods used in the 5x5 array is shown in Figure 40. The attachment method shown in Figure 40 uses a threaded end and nut to alleviate the need to enlarge the preexisting cavity in the graphite piston head.

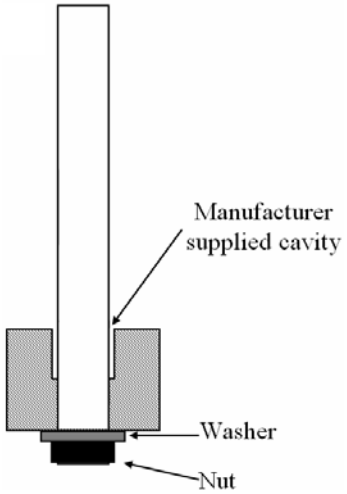


***Figure 40:*** *Improved piston head attachment method*

While the attachment method discussed in section 4.6 allows the piston rod to flex about its longitudinal axis the method shown in Figure 40 is significantly easier to manufacture and provides sufficient flexibility for practical applications of Digital Clay. Furthermore, the side loading on the piston head (section 4.7) as the piston moves upward is significantly reduced.

## 5.2 Salient Characteristics of Digital Clay

The compact 5x5 Digital Clay array of fluidic actuators is easily scalable. The main hindrance to the scalability of a single fluidic actuator was the size of the solenoid valves that were used during the characterization of the single fluidic actuator (chapters 2-4). However, such valves are inherently scaleable and can be fabricated at the micro-scale. It is anticipated that ultimately, the electronics boards attached to each actuator and the desired output force will be the limiting scalability factors. While the inclusion of a hydraulics system to drive the array demands the presence of two reservoirs and a pumping system, the lack of mechanical actuators (e.g. FEELEX, Chapter 1) enables a compact and scalable solution.

The present Digital Clay provides substantially improved position monitoring over previous tactile arrays (section 1.2-1.3) by using embedded absolute position sensors in each actuator rather than relying on external measurement devices or inferring position from integration of system parameters. The present approach not only yields a scalable tactile array, but provides a very modular solution in which each individual actuator contains all of the necessary hardware to be self functioning. This means that any

actuator in the array can be easily removed and replaced/relocated at any time without loss of accuracy and functionality. The array contains all necessary components for its operation in a neatly packaged base which integrates the fluid system with the drive and control electronics and communications.

## 5.3 Future System Improvements

The form of Digital Clay presented in this work provides the ability for a user to economically represent and interact with a desk-top sized topography through a remote software package. However, there are a number of improvements that can be made. While Digital Clay is functional with respect to position control, it does not contain the ability to measure the force effected by or on the pistons. Therefore, the inclusion of force measuring capabilities would greatly enhance the present design of Digital Clay.

The linear variable differential transformer chip attached to each actuator of the 5x5 array consumes approximately 40 mA. This current can be significantly reduced if a finer wire is used to build the variable core transformer (currently made with 34 gauge wire). A smaller diameter wire will also enable a higher sensitivity along with additional turns per unit length of the coil (section 3.1).

As noted in Chapter 3, the current VCT design suffers from reduced sensitivity at the end of the piston's range of motion (Figure 18 Chapter 3) because the piston rod is only partially immersed in the changing magnetic field of the primary coil. One way to mitigate this issue is to move the access hole in the glass tube closer to the top and

modify the insertion depth of the Teflon top seal as shown in Figure 41b. This modification would allow the VCT to be wound on a longer segment of the glass tube and therefore allow the piston rod to have a longer immersion length in the magnetic field of the VCT in the fully extended position (Figure 41b).

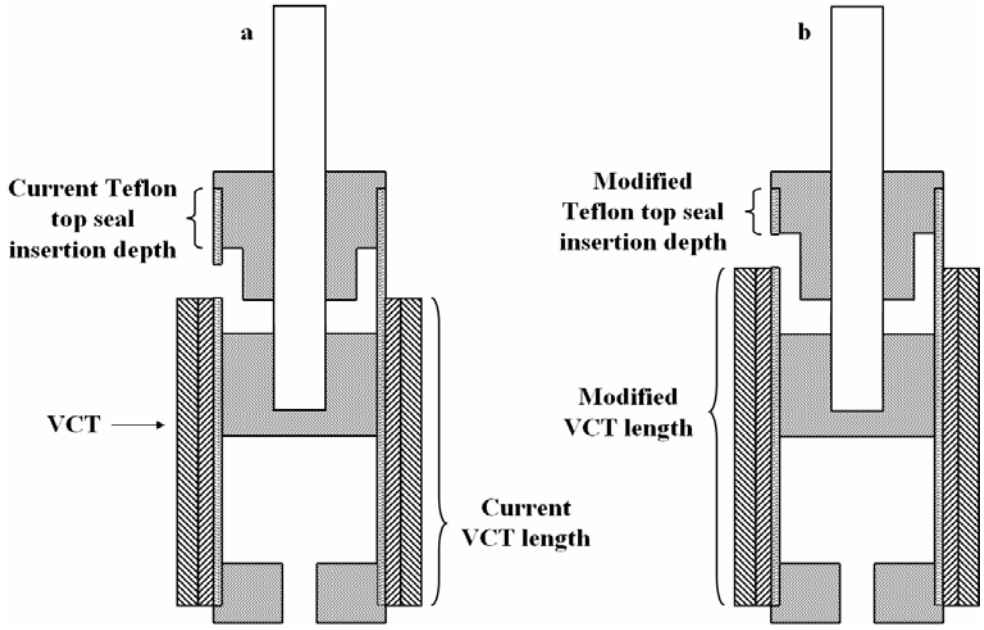


***Figure 41:*** *Current (a) and proposed (b) Teflon top seal and VCT*

Finally, the use of pulse width modulation for actuation of the valves would add the ability to control the solenoid valves proportionally, which would give the Digital Clay system an enhanced ability to display moving curved surfaces, and changing velocity trajectories.

## 5.4 Summary and Conclusions

Earlier tactile arrays or haptic sensors (sections 1.1-1.3) do not enable user interaction with a compact, highly accurate package through remote software. The present work has demonstrated the realization of these goals through the creation of Digital Clay that is

comprised of an array of interactively activated fluidic actuators. The present work has focused on the development and characterization of the performance of a prototypical fluidic actuator with embedded position sensing. Each actuator is comprised of a hydraulically-driven piston whose position is sensed by an embedded variable core transformer. The actuators are integrated with computer-controlled valves and an underlying base plate that is in fluidic communication with high and low-pressure fluid reservoirs. The system can be operated over a broad range of pressures and the resulting piston motion was characterized in detail including time based trajectory, velocity and acceleration. Pressure measurements sampled at various system locations were used to characterize the dynamics of the internal fluidics of the actuator and the surrounding system. The viscous losses in the system's fluidic channels were calculated and compared well with detailed pressure difference measurements. An embedded variable core transformer was developed and shown to be capable of accurately measuring the position of the piston. Although the error of the position as measured by the embedded sensor increases as the piston reaches its fully extended position, the overall error is still comparable to the conventional, external optical displacement measurements. Furthermore, the ability to integrate this sensor into each piston allows for modular, scalable design. The present work shows that the variable core transformer is ideally suited for a closed-loop proportional integral controller that was developed to monitor the desired position of each piston. The position measurements from the embedded position sensor were numerically differentiated in order to calculate the velocity and acceleration of the piston. The acceleration was then used in the calculation of the friction forces acting on the piston.

The fluidic actuator which was characterized in Chapters 2-4 was modified and used in the creation of a 5x5 array of actuators which is capable of remote shape display and interaction. While the piston mounting technique resulted in position dependent side loading during the piston motion it was possible to conceive a different mounting technique to alleviate this issue in Digital Clay arrays. Each actuator in the array is capable of lifting 345 grams (3.3 N) and holding 590 grams (5.8 N). Therefore, the array is capable of lifting and holding approximately 8.6 Kg and 14.8 Kg respectively.

Digital Clay presents an attractive design interface for the design and interaction with three dimensional objects. Using multiple arrays, Digital Clay will allow multiple users to "sculpt" a single digital model from multiple locations through physical interaction. This could give rise to rapid design decisions by allowing users to interact rapidly with underlying models instantly across large distances. Digital Clay also provides an alternative interface for the representation of objects for the visually impaired. One straightforward application of this type is the representation of mathematical functions. However, Digital Clay could also be used for the digitization of television and movie pictures to allow visually impaired users, as well as seeing users, the ability to feel what is normally perceived as a 2-D image.

# REFERENCES


Amato, I. (2001). Helping Doctors Feel Better. Technology Review. **104:** 65-71.

Brooks, F. P. J. O.-Y., Ming Batter, James J. Kilpatrick, P. Jerome (1990). "Project GROPE - Haptic Displays for Scientific Visualization." Computer Graphics **24**(4): 177-185.

Chan, A. M., Karon; McGrenere, Joanna (2005). Learning and Identifying Hapric Icons under Workload. Symposium on Eurohaptics Conference, Pisa, Italy.

Fearing, R. S., G. Moy, and E. Tan (1997). Some Basic Issues in Teletaction. IEEE International Conference on Tobotics and Automation, Albuquerque, New Mexico, USA

Figliola, R. S. B., Donald, E. (2000). Theory and Design for Mechanical Measurements, John Wiley & Sons, Inc.

Goertz, R. (1952). "Fundamentals of General-Purpose Remote Manipulators." Nucleonics **10**(11): 36-42.

Goertz, R. (1954). "Electrically Controlled Manipulator." Nucleonics **12**(11): 46-47.

Gray, B. L. F., Ronald S. (1996). A Surface Micromachined Microtactile Sensor Array. IEEE International Conference on Robotics and Automation, Minneapolis, MN.

Howe, R. D. P., WIlliam J. Kontarinis,Dimitrios A. Son,Jae S. (1995). "Remote Palpation Technology." IEEE Engineering in Medicine and Biology **14**(3): 318-323.

Hull, H. L. (1952). "Remote Control Engineering." Nucleonics **10**(11): 34-35.

Iwata, H. Y., Hiroaki Nakaizumi,Fumitaka Kawamura,Ryo (2001). Project FEELEX: Adding Haptic Surface to Graphics. Siggraph, Los Angeles, CA, USA.

Jost, D. A. (1997). "Mechanoreceptor". The American Heritage College Dictionary. K. Ellis. Boston, MA, Houghton Mifflin Company.

Kaczmarek, K. A. T., Mitchell E.; Bach-y-Rita, Paul (1994). Electrotactile Haptic Display on the Fingertips: Preliminary Results. 16th Annual International Conference of the IEEE Biomedical Engineers, Baltimore, MD.

Kaczmarek, K. A. W., John G. Bach-y-Rita,Paul Tompkins,Willis J. (1991). "Electrotactile and Vibrotactile Displays for Sensory Substitution Systems." IEEE Transactions on Biomedical Engineering **38**(1): 1-16.

Kikuuwe, R. S., Akihito; Mochiyama, Hiromi; Takesue, Nayoyuki; Fujimoto, Hideo (2004). A tactile sensor capable of mechanical adaption and its use as a surface deflection detector. IEEE Sensors, Vienna, Austria.

Kron, A. S., Gunther (2005). Haptic Telepresent Control Technology Applied to Dospisal of Explosive Ordnances: Principles and Experimental Results. IEEE International Symposium on Industrial Electronics, Durrovnik, Croatia.

Kumar, V. (2001). Introduction to Robotics**:** 1-21.

Linvill, J. G. B., J.C. (1966). A Direct Translation Reading Aid for the Blind.

Melli-Huber, J. W., B.; Fisch, A.; Nikitczuk, J; Mavroids, C; Wampler, C. (2003). Electro-rheological fluidic actuators for haptic vehicular instrumen controls. Symposium on Haptic Interfaces for Virtual Envitonment and Teleoperator Systems, Los Angeles, CA.

Nakashige, M. H., K.; Hirose, M.; (2004). Linear actuator for high-resolution tactile display. IEEE International Workship on Robot and Human Interactive Communication, Kurashiki, Okayama Japan.

Nakatani, M. K., Hiroyuki Sekiguchi,Dairoku Kawakami,Naoki Tachi,Susumu (2003). 3D Form Display with Shape Memory Alloy. International Conference on Artificial Reality and Telexistence, Tokyo, Japan.

Perry, T. S. (1994). The Media Event. IEEE Spectrum. **31:** 21.

Press, W. H. T., Saul A. Vetterling,William T. Flannery,Brian P. (1992). Numerical Recipes in C. New York, Press Syndicate of the University of Cambridge.

Rizzoni, G. (2000). Principles and Applications of Electrical Engineering. Boston, McGraw Hill.

Robles-De-La-Torre, G. (2006). "The Importance of the sense of touch in virtual and real environments." IEEE Multimedia **13**(3): 24-30.

Rossignac, J. A., Mark Book,Wayne J. Glezer,Ari Ebert-Uphoff,Imme Shaw,Chris Rosen,David Askins,Stephen Bai,Jing Bosscher,Paul Gargus,Joshua Kim,ByungMoon Llamas,Ignacio Nguyen,Austina Yuan,Guang Zhu,Haihong (2003). Finger Sculpting with Digital Clay: 3D Shape Input and Output through a Computer-Controlled Real Surface. Shape Modeling International, Seoul, Korea.

Srinivasan, M. A. B., Cagatay (1997). "Haptics in virtual environments: taxonomy, research status, and challenges." Computers & Graphics **21**(4): 393-404.

Stone, R. J. (2001). Haptic Feedback: A Brief History, From Teleoperation to Virtual Reality. Haptic human computer interaction: first international workshop, Glasqow, UK.

Taylor, P. M. H.-S., A.; Varley, C. J.; (1996). An Electrorheological Fluid-based Tactile Array for Virtual Environments. IEEE Conference on Robotics and Automation, Minneapolis, MN.

Welsby, V. G. (1950). The Theory and Design of Inductance Coils. London, MacDonald & Co. Ltd.

Yong, L. S. Y., Wong Hong Ang,Marcelo Jr. (1998). Robot Task Execution with Telepresence Using Virtual Reality Technology. International Conference on Mechatronics. Hshinchu Taiwan.

Young, H. D. F., Roger A. (1996). University Physics, Addison-Wesley Publishing Company, Inc.

Zhu, H. (2005). Practical Structural Design and Control for Digital Clay. Woodruff School of Mechanical Engineering. Atlanta, Georgia Institute of Technology. **Doctor of Philosophy:** 168.